Nuclear Fusion 59, 2019

https://doi.org/10.1088/1741-4326/ab3f7a

Characterisation of Highly Radiating Neon Seeded Plasmas in JET-ILW

S Glöggler[1,2], M Wischmeier[1], E Fable[1], E R Solano[3], M Sertoli[1,8], M Bernert[1], G Calabrò[4], M Chernyshova[5], A Huber[6], E Kowalska-Strzęciwilk[5], C Lowry[7], E de la Luna[3], C F Maggi[8], U Stroth[1,2], H J Sun[8], M L Reinke[9], S Wiesen[6] and JET Contributors*

[1]Max Planck Institute for Plasma Physics, Boltzmannstraße 2, 85748 Garching bei München, Germany
[2]Physik-Department E28, Technische Universität München, 85747 Garching bei München, Germany
[3]Laboratorio Nacional de Fusión, CIEMAT, 28040 Madrid, Spain
[4]Department of Economics, Engineering, Society and Business Organization (DEIm), University of Tuscia, Largo dell'Università snc, 01100 Viterbo, Italy
[5]Institute of Plasma Physics and Laser Microfusion, 23 Hery Street, 01-497 Warsaw, Poland
[6]Forschungszentrum Jülich GmbH, Institut für Energie- und Klimaforschung - Plasmaphysik, 52425 Jülich, Germany
[7]European Commission, 1049 Brussels, Belgium
[8]CCFE, Culham Science Centre, Abingdon, OX14 3DB, UK
[9]Oak Ridge National Laboratory, Oak Ridge, TN 37831, USA
*See the author list of E. Joffrin et al. accepted for publication in Nuclear Fusion Special issue 2019, https://doi.org/10.1088/1741-4326/ab2276

E-mail: stephan.gloeggler@ipp.mpg.de

August 2019

Characterisation of Highly Radiating Neon Seeded Plasmas in JET-ILW

S Glöggler[1,2], M Wischmeier[1], E Fable[1], E R Solano[3], M Sertoli[1,8], M Bernert[1], G Calabrò[4], M Chernyshova[5], A Huber[6], E Kowalska-Strzęciwilk[5], C Lowry[7], E de la Luna[3], C F Maggi[8], U Stroth[1,2], H J Sun[8], M L Reinke[9], S Wiesen[6] and JET Contributors*

[1]Max Planck Institute for Plasma Physics, Boltzmannstraße 2, 85748 Garching bei München, Germany
[2]Physik-Department E28, Technische Universität München, 85747 Garching bei München, Germany
[3]Laboratorio Nacional de Fusión, CIEMAT, 28040 Madrid, Spain
[4]Department of Economics, Engineering, Society and Business Organization (DEIm), University of Tuscia, Largo dell'Università snc, 01100 Viterbo, Italy
[5]Institute of Plasma Physics and Laser Microfusion, 23 Hery Street, 01-497 Warsaw, Poland
[6]Forschungszentrum Jülich GmbH, Institut für Energie- und Klimaforschung - Plasmaphysik, 52425 Jülich, Germany
[7]European Commission, 1049 Brussels, Belgium
[8]CCFE, Culham Science Centre, Abingdon, OX14 3DB, UK
[9]Oak Ridge National Laboratory, Oak Ridge, TN 37831, USA
*See the author list of E. Joffrin et al. accepted for publication in Nuclear Fusion Special issue 2019, https://doi.org/10.1088/1741-4326/ab2276

E-mail: stephan.gloeggler@ipp.mpg.de

August 2019

Abstract. To study the impact of strong impurity radiation on the energy confinement and the discharge stability, at JET-ILW dedicated high-density, highly heated experiments with neon seeding have been performed. In these experiments an increase of radiation in the core and especially the pedestal region and a characteristic strong X-point radiator inside the confined region have been observed. The increased radiation inside the separatrix had no impact on the energy confinement. Only at the highest neon puff rates and highest heating powers (29 MW) a weak H-mode without back-transitions to L-mode (M-mode) could be achieved, while at lower heating powers or seeding levels L-modes and oscillations between H-mode and L-mode could be observed. In H-mode, at highest neon seeding levels the targets are in complete detachment. A degradation of the pedestal density profile was observed when neon was seeded. A correlation between this density pedestal degradation, the appearance of an X-point radiator and the detachment of the targets was found in neon seeded H-mode pulses.

In ASTRA-TGLF core transport simulations it could be shown that the increase of the electron temperature in the core with neon seeding is attributed to a partial

stabilisation of ITG modes.

Keywords: Plasma, Fusion, JET, Neon, Radiation

1. Introduction

In future fusion devices like DEMO radiation from impurities is required to meet the tight constraints set by the material limits of the divertor target plates [1, 2]. To keep the heat flux density onto the target below $5-10\,\mathrm{MW/m^2}$, more than 95 % [1, 2] of the total heating power of around 450 MW [3, 4] have to be dissipated in DEMO with an ITER-like divertor configuration. Because the dissipative capabilities of the scrape-off layer (SOL) can be estimated to be about $P_{\mathrm{rad,SOL}} \approx 100\,\mathrm{MW}$, over 70 % [2, 3] of the power have to be radiated inside the separatrix. Such increased radiation levels are achieved by deliberate puffing of impurity gases into the plasma. However, impurities in the core plasma can cause fuel dilution and increased core radiation, leading to limitations in the operational space or even to the suppression of ignition [5, 6].

In order to reduce the energy deposited on the target not only low target plasma temperatures of below 4 eV [1] but also low particle fluxes towards the target are required. Such conditions can be found in the so called detached regime. A detached regime is characterised by decreased heat flux at the targets and a pressure loss between the mid-plane and the targets [7]. A future fusion device must operate with detached targets. Additionally it must have a sufficiently large energy confinement time τ_{E}. In current experiments high confinement times are achieved in the high confinement mode (H-mode). The seeding of impurities into the plasma might at the one hand lead to detached divertor targets but on the other hand it might as well decrease the power transported over the separatrix P_{SOL} below a threshold value P_{LH}, causing the plasma to not being in H-mode anymore.

In the past, experiments with nitrogen, neon, argon, and krypton at ASDEX Upgrade and JET have shown high radiating scenarios with detached divertors and a characteristically high radiaton power density at the X-point [8, 9, 10]. At JET experiments with comparably small seeding of neon [11] and nitrogen [12] have been performed as well. While nitrogen was shown to radiate primarily in the divertor, neon radiated close to the separatrix and in the pedestal region of JET. In this work, high radiation neon seeded experiments have been performed at JET with ITER-like wall (ILW; i.e. with tungsten divertor and beryllium main chamber walls). They allow to investigate the effect of neon radiation on the confinement, the poloidal radiation distribution, and ways to achieve a high radiative power fraction, which is the ratio $f_{\mathrm{rad}} = P_{\mathrm{rad}}/P_{\mathrm{heat}}$ of radiated power to heating power.

The paper is organised as follows: Section 2 will give an overview over the set-up of the neon seeded discharges and present the findings made at high neon seeding rates and different levels of heating power. One of these findings, the increased energy confinement time τ_{E}, is examined in section 3 using the ASTRA-TGLF transport code. Section 4 presents experimental observations of the impurity content of the core plasma. The relation between core and edge radiation as well as a correlation of the X-point radiator with the pedestal density degradation and detachment of the targets in neon seeded H/M-modes are studied in section 5. The paper is concluded with a discussion of the

results in section 6.

2. Characterisation of Neon Seeded JET Discharges

The neon seeded experiments were performed at different levels of deuterium puffs (0.2–$1.0 \cdot 10^{23}$ el/s) into the divertor scrape-off layer (SOL) and neon puffs (0.4–$2.2 \cdot 10^{22}$ el/s) in the private flux region (PFR) as well as at a broad range of heating powers between 14 and 29 MW (see Fig. 1; for $P_{\mathrm{heat}} < 20$ MW with only NBI heating, for $P_{\mathrm{heat}} > 20$ MW with additional ICRH). This section presents results of 3 experiments which are characteristic for their respective heating power at comparably high neon seeding rates: low power heating at 15 MW in section 2.1, medium power at 19 MW in section 2.2, and high power at 29 MW in section 2.3. The conditions for a transition to a regime without large (type-I) edge-localised modes (ELMs) are discussed in section 2.4.

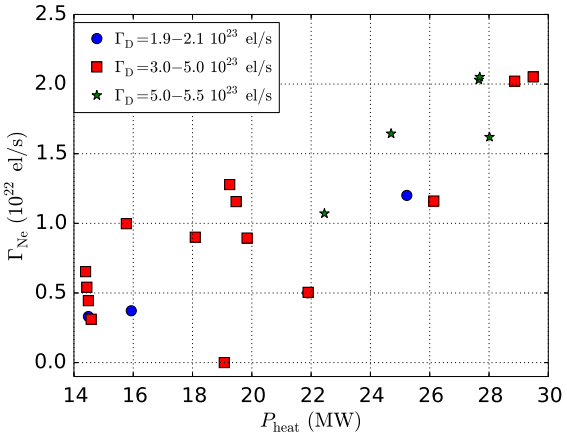

Figure 1. *Operational space of the examined neon seeded JET-ILW discharges, described by total heating power P_{heat} and neon puff rate Γ_{Ne}. The colour coding indicates the 3 stages of the deuterium puff rate Γ_{D}.*

The discharges were performed at similar poloidal flux profiles (see Fig. 2a) in vertical target (VT) configuration, with the strike lines lying on the vertical tiles 3 (inner) and 7 (outer). Even though the VT configuration was shown to have a lower confinement than the configuration with the strike points in the corner [13, 14], it was chosen because it leads to increased re-ionisation in the divertor, volumetric energy losses and thus to decreased power fluxes on the targets [15, 16]. Operation with vertical targets is therefore considered to be relevant for ITER and other future machines. The plasma current $I_{\mathrm{P}} = -2.5$ MA and toroidal magnetic field strength $B_{\mathrm{T}} = -2.65$ T were kept constant throughout all the discharges. The Greenwald density in all the discharges was around $n_{\mathrm{G}} = 0.9 \cdot 10^{20}\,\mathrm{m}^{-3}$. With a maximum radiative power fraction of $f_{\mathrm{rad,max,Ne}} = 0.66$ the discharges remained slightly below the JET maximum of $f_{\mathrm{rad,max,JET}} = 0.75$, which has been achieved with nitrogen seeding under completely detached conditions [10].

The low maximum value of f_{rad} even under completely detached conditions indicates a discrepancy in the power balance at JET which is currently under investigation [17, 18].

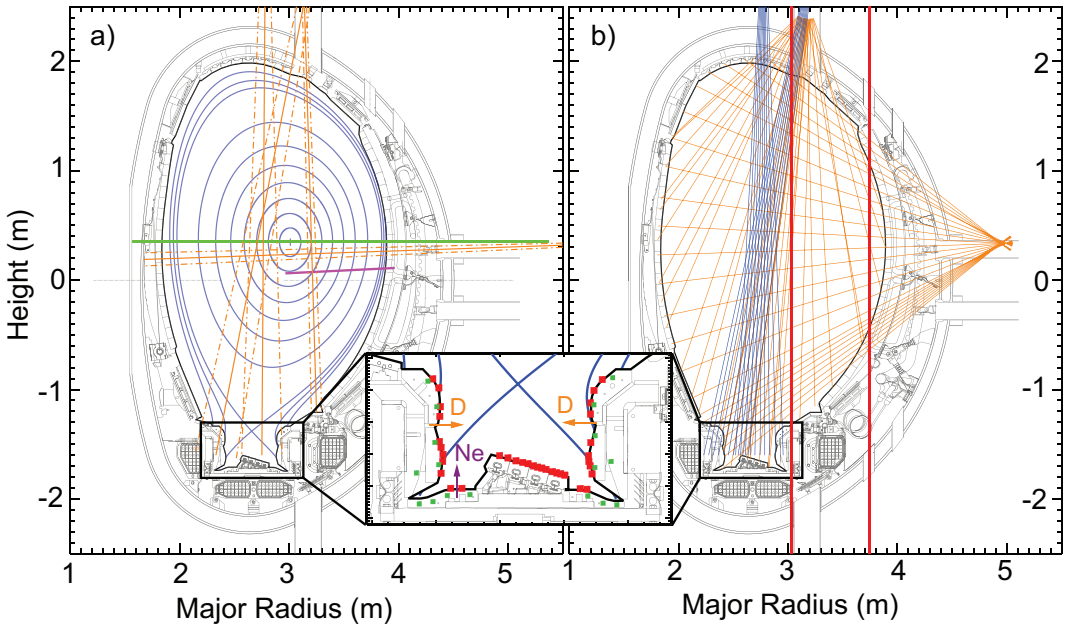

Figure 2. *a) Typical magnetic flux surfaces (blue), Visible Light Spectrometer lines of sight of the global array (orange), High Resolution Thomson Scattering (magenta), Electron Cyclotron Emission (green). b) Horizontal and vertical bolometer lines of sight (orange), Visible Light Spectrometer lines of sight of the divertor array (blue), and channels 3 (core) and 4 (edge) of the infrared interferometer system (red). In the enlarged area: Divertor Langmuir probes (red), divertor thermocouples (green), and locations of deuterium (orange) and neon puffs (purple).*

In the zoomed part of Fig. 2 the poloidal positions of the divertor Langmuir probes (LPs, red) are shown. They were run in single mode with sweeping voltage. The divertor thermocouples (TCs, green) are used to measure the temperature of the divertor tiles. Deuterium is puffed from the Gas Introduction Modules (GIMs) 10 and 12 (orange arrows) at the vertical targets into the SOL while neon was puffed from GIM 11 (purple arrow) at the horizontal tile 4 into the private flux region (PFR). The JET divertor GIM's points of gas entry are placed toroidally symmetric. The temperature and density profiles are measured by the High Resolution Thomson Scattering diagnostic [19, 20] (HRTS, magenta line in Fig. 2a). Due to uncertainties in the magnetic field reconstruction and the separatrix position it is common practice to radially shift HRTS profiles to get a separatrix electron temperature of around 100 eV in H-mode. An estimation of the separatrix electron temperature based on the Spitzer-Härm conductivity and the two-point model [21] (method as applied in [22]) for some of the discharges presented here showed that it is legit to assume separatrix electron temperatures of around 100–130 eV in H-mode. For higher time-resolved temperature

profiles measurements of the electron cyclotron emission radiometer [23] (ECE, green) can be analysed. In particular in this paper it is used to analyse oscillations at the pedestal position. The line-averaged effective charge state $Z_{\mathrm{eff}} = \sum_Z n_Z Z^2/n_{\mathrm{e}}$ (with n_Z being the density of impurity ions of charge state Z and n_{e} the electron density) is derived from the Bremsstrahlung signal of the horizontal line of sight (LOS) in the global Visible Light Spectrometer (VLS, blue) array and the HRTS profiles of electron density n_{e} and electron temperature T_{e} (similar as in [24]).

For JET Pulse Number (JPN) 92118 with a neon seeding rate of $\Gamma_{\mathrm{Ne}} = 1.2 \cdot 10^{22}\,\mathrm{el/s}$ and a heating power of $P_{\mathrm{heat}} = 23\,\mathrm{MW}$ core and pedestal ion temperatures were determined by charge exchange emission spectroscopy of fully ionised neon ions. It could be shown by these T_{i} profiles and T_{e} profiles from HRTS that the assumption $T_{\mathrm{i}} = T_{\mathrm{e}}$ is justified over the entire radial profile, as well for an unseeded as for a neon seeded time-point. The temperature equality results from the high plasma density in this discharge. The neon puffing does not seem to have an impact on this equality, neither in the core nor in the edge. The neon seeding rate in JPN 92118 was equal or higher than in most discharges presented in this article. Due to their high densities, it will be assumed in the following that $T_{\mathrm{i}} = T_{\mathrm{e}}$ is true for all of discharges presented in this article.

In Fig. 2b the LOS of the horizontal and vertical bolometers are shown (in orange) which are used for a tomographic reconstruction of the poloidal radiation distribution [25, 26, 27]. The bolometer divertor array (not shown) was not used for this reconstructions. The total radiated power, P_{rad}, can be calculated from such a tomographic reconstruction. Due to the computational expenses of a full tomographic reconstruction a weighted sum of vertical bolometer channel measurements is calculated in order to receive a time-resolved signal of P_{rad}. The blue lines indicate the LOS of the divertor array of the visible light spectrometer which measure the W I, D_α and Be II lines, used to identify edge localised modes (ELMs) and transitions between high (H-mode) and low confinement mode (L-mode). Also, an edge channel of the infrared interferometer system [28] (red line) is used to observe the characteristic increase of the pedestal density due to the formation of a pedestal during the transition from L-mode to H-mode.

*2.1. Low Heating Power (*15 MW*)*

In the least heated discharge, JPN 87196, the heating power was 15 MW (see Fig. 3). The plasma is in an ELMy H-mode phase when the neon puff begins to affect the plasma (from around $t = 10.0\,\mathrm{s}$ on). After $t = 11.0\,\mathrm{s}$ ELMs are not observed anymore. From the radial T_{e} and n_{e} profiles (see Fig. 4) a transition from H-mode to L-mode can hardly be derived, also in the line-integrated density no major change could be observed. The presence of ELMs before $t = 11.0\,\mathrm{s}$ and the absence of ELMs afterwards indicate, though, that the plasma underwent a transition from a highly degraded type-III ELMy H-mode to L-mode. The energy confinement time $\tau_{\mathrm{E}} = \frac{W_{\mathrm{th}}}{P_{\mathrm{heat}} - \mathrm{d}W_{\mathrm{th}}/\mathrm{d}t}$ (with W_{th} being the

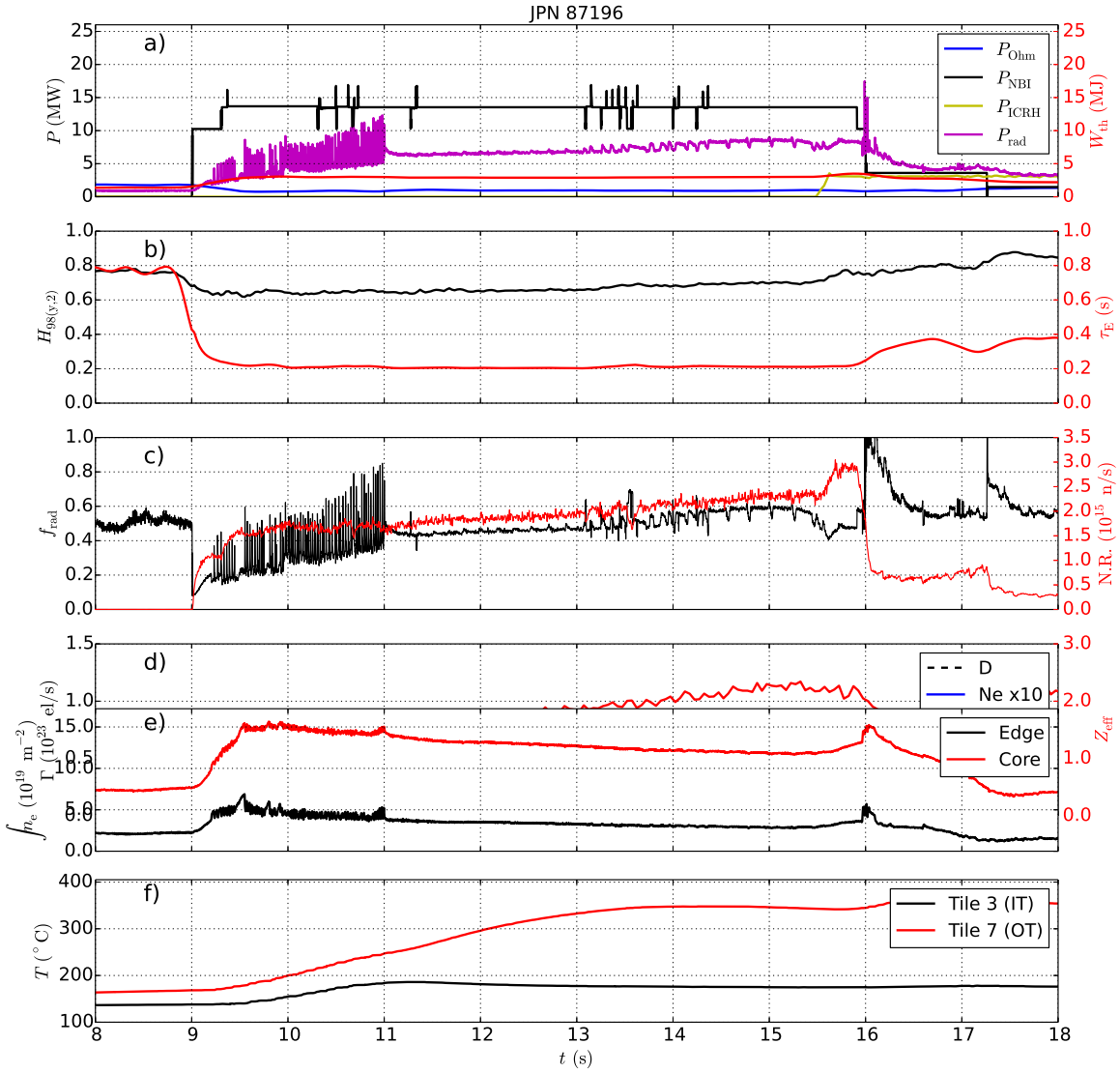

Figure 3. *Timetraces of JPN 87196, a low power discharge ($P_{\rm heat} = 15\,$MW) with three neon seeding steps. From top: a) heating and radiation powers, energy content $W_{\rm th}$; b) energy confinement time $\tau_{\rm E}$ and $H_{98({\rm y},2)}$; c) $f_{\rm rad}$ and neutron rate; d) deuterium and neon puff strengths, $Z_{\rm eff}$; e) the line-integrated density from an edge and a core IR interferometry channel (see Fig. 2); f) temperatures of thermocouples close to the strike points in the vertical tiles 3 and 7. The neon puff, starting at $t = 9.5\,$s, begins to affect the plasma at around $t = 10.0\,$s, indicated by the increasing $Z_{\rm eff}$. From $t = 11.0\,$s on the plasma is in L-mode that only ends at the end of the discharge.*

thermal energy stored in the plasma and $P_{\rm heat}$ the injected heating power which in the examined JET discharges is very close to the absorbed heating power) does not decrease during this transition. The same applies for the confinement factor $H_{98({\rm y},2)} = \tau_{\rm E}/\tau_{98({\rm y},2)}$

(with the energy confinement time $\tau_{98(y,2)}$ according to the IPB98(y,2) scaling [29]) which remains at a constant value of $H_{98(y,2)} \approx 0.6$. It was observed, not only in this discharge but in all discharges presented in the following, that τ_E and $H_{98(y,2)}$ were barely changed with the onset of neon puffing. It has to be taken into consideration that their values are comparably low already at the beginning of the discharge when no neon was seeded. This can be attributed to the high deuterium puffing rates that were applied to increase the neutral pressure in the divertor. High D_2 puffs have been shown to decrease pedestal temperature [13] and $H_{98(y,2)}$ [30, 31].

The region of major radiation power density is located at the high-field side (HFS) before the neon puff and after it takes effect until $t = 14.2\,\mathrm{s}$. The radiation power density is more than double with neon seeding and additionally the radiation inside the confined region close to the X-point is increased as well (see Fig. 5). From $t = 14.2\,\mathrm{s}$ until after the end of the neon puff, the highest radiation power density can be measured around to the X-point, also inside the separatrix. On the first neon seeding step the radiative power fraction $f_{\mathrm{rad}} \approx 0.5$ is lower than values that have been achieved in other experiments (up to 0.75 in nitrogen seeded discharges, up to 0.66 with neon). Only on the fourth neon seeding step, a radiative power fraction of around 0.65 is reached.

From the divertor thermocouples located in the inner target tiles an increase of about 50 °C up to $t = 11\,s$ is measured, followed by a slight temperature drop. At the outer target tiles a significant increase in temperature of up to 290 °C until $t = 14\,s$ could be measured. This is in the same order of magnitude as the unseeded reference discharge JPN 84884 ($P_{\mathrm{heat}} = 19\,\mathrm{MW}$) where an increase of about 270 °C could be measured. The temperature increase in both discharges is stopped only by the end of the discharge. These data give a hint that the inner target might be detached and the outer target attached until $t = 14\,s$. However, a decreasing temperature can only indicate a reduced heat flux compared to the time window in which the temperature is increasing but not necessarily that the heat flux is reduced enough to characterise detachment. The Langmuir probes at the targets (see Fig. 6) show that the inner target is detached after the impurity puff, but instead the peak electron temperature at the outer target increases from about 20 to 35 eV. This means that still a rather large amount of power is deposited on the outer divertor target and, thus, that the outer target is still attached during the L-mode phase with neon seeding.

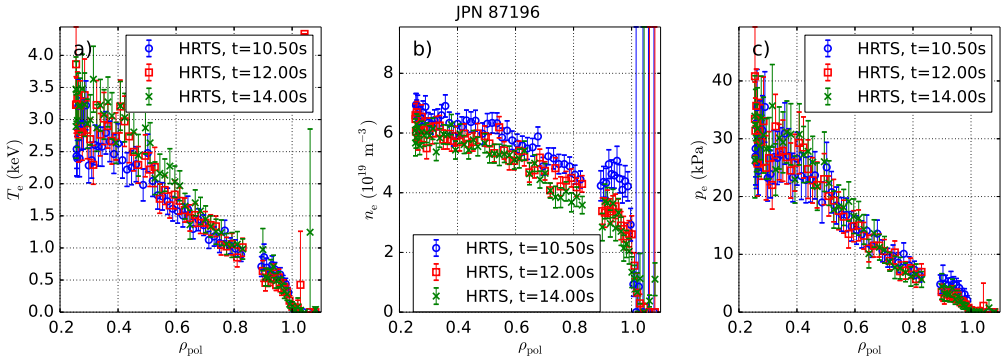

Figure 4. *Median radial a) electron temperature, b) electron density, and c) electron pressure profiles in the unseeded phase (blue), on the second step (red) and on the fourth step of neon seeding (green) of JPN 87196 ($P_{heat} = 15$ MW). A minor increase of the core T_e and a slight degradation of the pedestal n_e can be observed the more neon is seeded. As the profiles for the unseeded and the seeded time points are very similar, there is no indication that the neon puff might have caused a transition from H-mode to L-mode.*

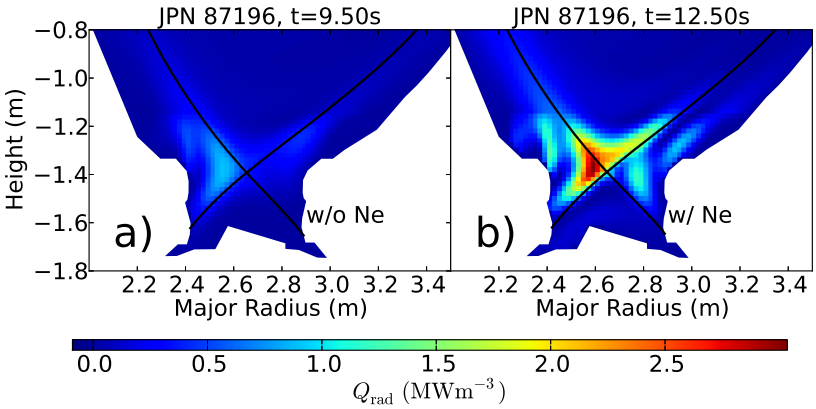

Figure 5. *Tomographic reconstructions of bolometer data of a) an unseeded and b) a neon seeded phase of JPN 87196 ($P_{heat} = 15$ MW). The neon puffing causes the radiation power density at the high-field side to increase but the poloidal distribution remains similar.*

2.2. Medium Heating Power (19 MW)

The medium power discharge, JPN 85443, has a heating power of 19 MW (see Fig. 7). Until after the beginning of the neon puff at $t = 10.5$ s, the discharge is found to be in ELMy H-mode with a transition from type-I to type-III ELMs at $t = 11.0$ s. At $t = 11.4$ s, the discharge undergoes a transition back to L-mode and reaches again H-mode at $t = 11.6$ s, which can be seen in the D_α signal (see Fig. 8a). In this second phase, no ELMs can be detected and instead a regular oscillation at 1–2 kHz can be seen in the D_α signal. In a spectrogram (see Fig. 8b) of a poloidal Mirnov coil above the

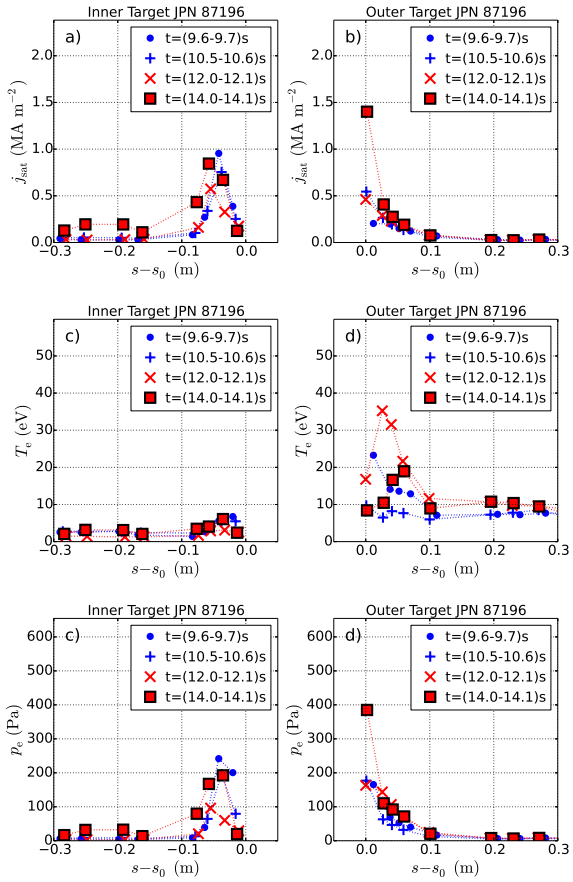

Figure 6. *Time-averaged (median) target profiles for ion saturation current j_{sat} (top), target electron temperature T_{e} (middle) and electron pressure p_{e} (bottom) at the inner (left) and outer (right) target of pulse 87196 ($P_{\mathrm{heat}} = 15\,\mathrm{MW}$). The coordinate $s - s_0$ marks the LP positions along the target with respect to the respective strike point. The inner target first detaches with more neon seeded (blue points: H-mode; red points: L-mode), but on the fourth neon step p_{e} and j_{sat} increase again to the initial values. The outer target is attached through the whole discharge, even though on the fourth neon seeding step the temperature is decreasing.*

inner divertor periodic oscillations at 1–2 kHz can be observed which is a characteristic indicator for an M-mode at JET [32].

An M-mode is a weak ELM-less H-mode regime found at JET [33, 34]. It is considered to be intermediate between L-mode and H-mode. It can typically be observed right after an L-H transition. In an M-mode a typical $n = 0$, $m = 1$ magnetic oscillation can be observed, e.g. by pedestal, SOL, and divertor measurements [32]. It has to be distinguished from type-III ELMs which are less periodical than the oscillation associated to the M-mode [32]. The M-mode is similar (or equal) to plasma states close to the L-H transition described in other experiments, e.g. at ASDEX Upgrade it is called I-phase [35, 36], at EAST [37] and HL-2A [38] it is described as a Limit Cycle

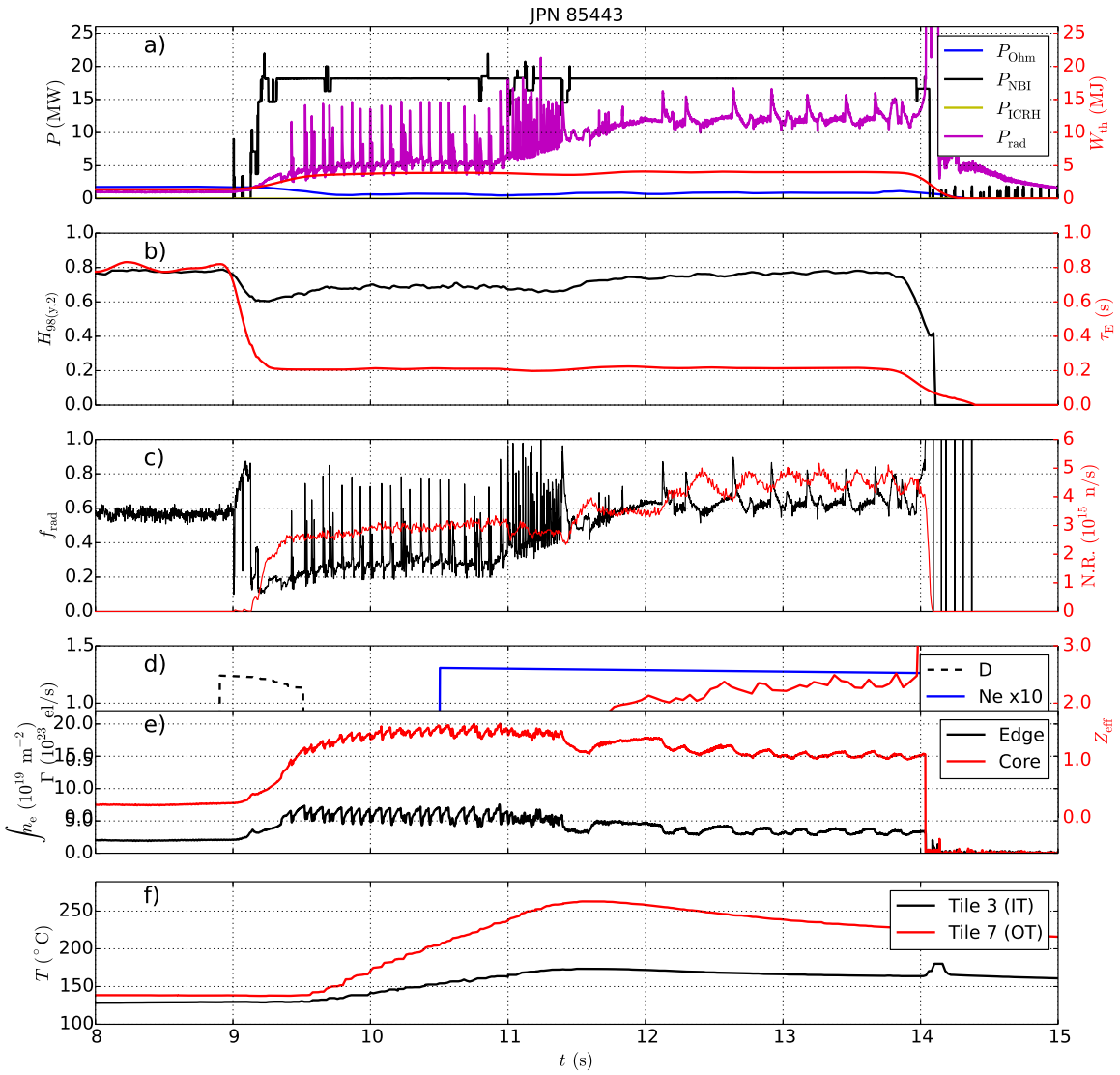

Figure 7. *Timetraces of JPN 85443, a medium power discharge (P_{heat} = 19 MW) with strong neon seeding. Quantities as described in Fig. 3. The neon puff (starting at $t = 10.5$ s) causes the plasma to go from type-I to type-III ELMs at $t = 11.0$ s first, followed by an L-mode phase and finally a transition to M-mode at $t = 12.0$ s, interrupted by transient back-transitions to L-mode.*

Oscillation. The I-phase appears prior to all L-H transitions and exhibits Limit Cycle Oscillations which are considered to be related to type-III ELMs [39]. M-mode and I-phase are widely considered identical [40, 32]. For the present study the M-mode is considered to be indicative for a situation where the power flux through the separatrix is close to the L-H threshold power.

In Fig. 8a the transition from a type-III ELMy H-mode (until $t = 11.4$ s) to L-mode and to M-mode (at $t = 11.6$ s) can be seen in the D_α signal (a rapid increase of the

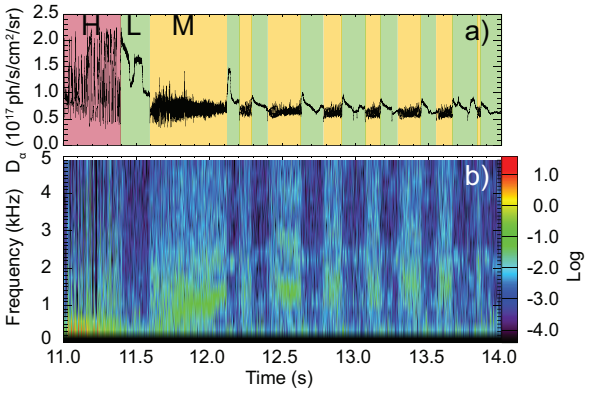

Figure 8. *a) D_α signal from the inner divertor of JPN 85443 ($P_{\mathrm{heat}} = 19\,\mathrm{MW}$). b) FFT spectrogram of poloidal Mirnov coil I803 (located at the lower HFS) for the neon seeded phase of JPN 85443. The oscillation at 1–2 kHz indicates that the plasma is in M-mode. Up to $t = 11.3\,\mathrm{s}$ ELMs can be seen until the plasma transits to L-mode and then to M-mode. In the following, further transitions to L-mode (characterised by a peaking in the D_α signal) and back to M-mode can be observed.*

D_α signal determines the transition to an L-mode while a drop suggest a transition to H-mode or M-mode). In the following, the M-mode phases are interrupted by transient back-transitions to L-mode. The following scheme for the M-L-M transitions is proposed [9]: It is assumed that with the characteristically increasing density in M-mode compared to L-mode the radiation is increased and hence the power transported over the separatrix, P_{SOL}, is decreased until it is below the L-H threshold power, P_{LH}. An increased outward transport of neon during the L-mode phase, causing a reduction of radiation and an increase of P_{SOL} (or of $Q_{\mathrm{i,edge}}$, according to [41]) above the L-H threshold again, might be a possible explanation for the back-transition to H-mode. A similar transport cycle was reported with krypton seeding at JET in order to describe dithering between H-mode and L-mode [9]. In the experiments presented here it was observed that the back-transitions to H-mode are triggered by sawtooth crashes.

From the poloidal reconstruction of the bolometer signals it can be seen that after the beginning of the neon seeding in JPN 85443 the region of the strongest radiation power density is shifted from the HFS to the X-point, inside the confined region (see Fig. 9). This phenomenon has been observed in previous experiments with nitrogen and neon seeding on ASDEX Upgrade and JET [8, 9, 10].

The energy confinement time remains constant with neon seeding. In contrast to the discharge with 15 MW heating power, where the radial density and temperature profiles and hence the energy confinement time were barely altered with neon seeded (see Fig. 4), clear changes can be observed in the radial profiles of JPN 85443 at a heating power of 19 MW: The electron density pedestal is strongly degraded (from $n_{\mathrm{e}} = 6 \cdot 10^{19}\,\mathrm{m}^{-3}$ to $2.5 \cdot 10^{19}\,\mathrm{m}^{-3}$ at the pedestal top position $\rho_{\mathrm{pol}} \approx 0.95$) after the onset of the neon puff but due to a steeper gradient the core density remains constant (see Fig.

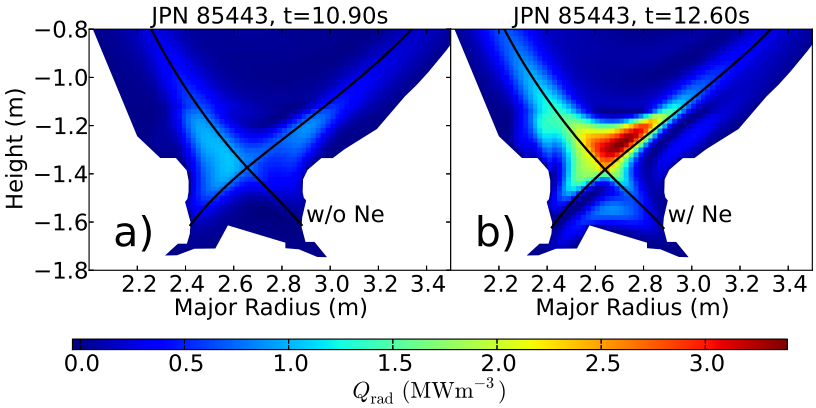

Figure 9. *Tomographic reconstructions of bolometer data of a) an unseeded and b) a neon seeded phase of JPN 85443 ($P_{\mathrm{heat}} = 19\,\mathrm{MW}$). With neon puffing the region with highest radiation power density shifts from the HFS into the confined region close to the X-point.*

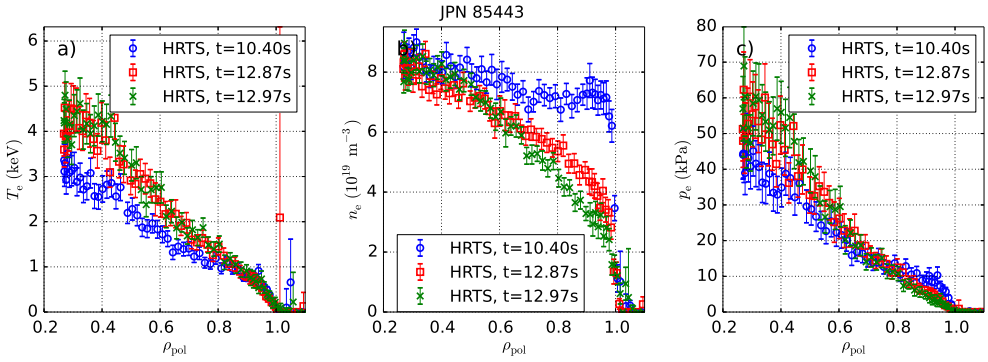

Figure 10. *Median radial profiles of JPN 85443 ($P_{\mathrm{heat}} = 19\,\mathrm{MW}$) as in Fig. 4. The n_e profile of the neon seeded time points (red and green) are strongly degraded with respect to the unseeded one (blue), especially in the pedestal region, and only reach the level of the unseeded time point in the core region. The density is slightly increased during M-mode phases (red) compared to L-mode phases (green). The T_e profiles have a similar shape in the pedestal region, while towards the core T_e is increased with neon seeding.*

10). T_e, however, increases in the core. The thermocouples in the inner target observe an increase of about 50 °C, at the outer target of around 100 °C until $t = 11.5\,\mathrm{s}$ when at both targets the temperatures start to decrease again when the neon takes effect. The targets are detached during M-mode phases with the observed X-point radiator but attached during L-mode (see Fig. 11, first described in [9]).

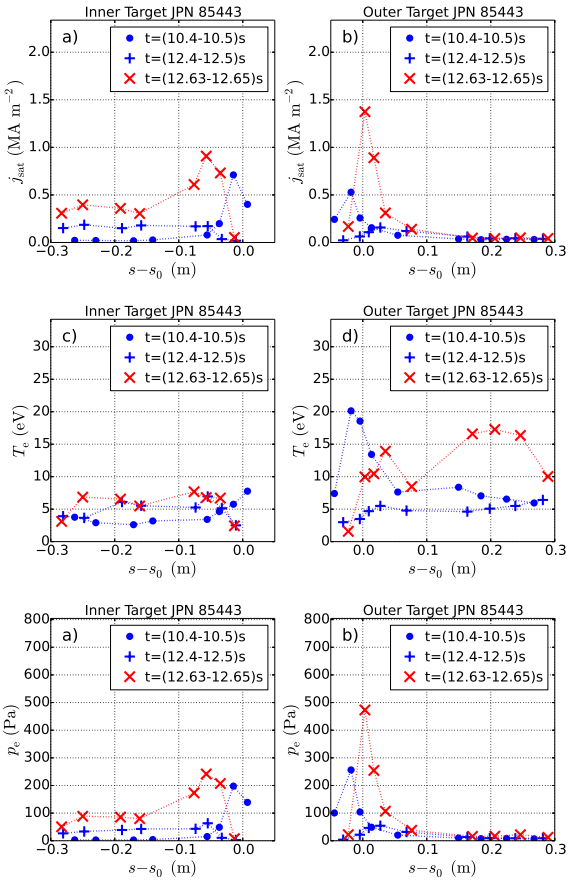

Figure 11. *Time-averaged (median) target profiles of JPN 85443 (P_{heat} = 19 MW) as in Fig. 6. In L-mode phases (red) the targets are attached while in H-mode (blue) they are in complete detachment.*

2.3. High Heating Power (29 MW)

In the high power discharge, JPN 92357 with 29 MW heating power, the neon puff was started during the ramp-up phase (see Fig. 12) in order to cool the divertor and prevent tungsten sputtering. For this reason the initial ELMy H-mode phase is shorter than in discharges presented above. At $t = 9.8$ s and 10.1 s short transient back-transitions to L-mode can be observed. Until shortly after the end of the neon puff at $t = 14.0$ s the ELMs vanish. Oscillations with a frequency of around 1.5 kHz can be found in the voltage signal of outer divertor pick-up coils and in the temperature signal of pedestal ECE channels, suggesting that the plasma is in M-mode. Since an M-mode usually is observed close to the L-H power threshold this implies that a large fraction of the heating power must be radiated inside the separatrix. Otherwise the discharge would be significantly over the L-H power threshold at the given heating power.

The discharge has a high radiative power fraction of $f_{\text{rad}} = 0.66$, while the highest radiation power density is at the X-point, inside the separatrix (see Fig. 13). Additionally, in this discharge it can be found that the radiation of the plasma centre

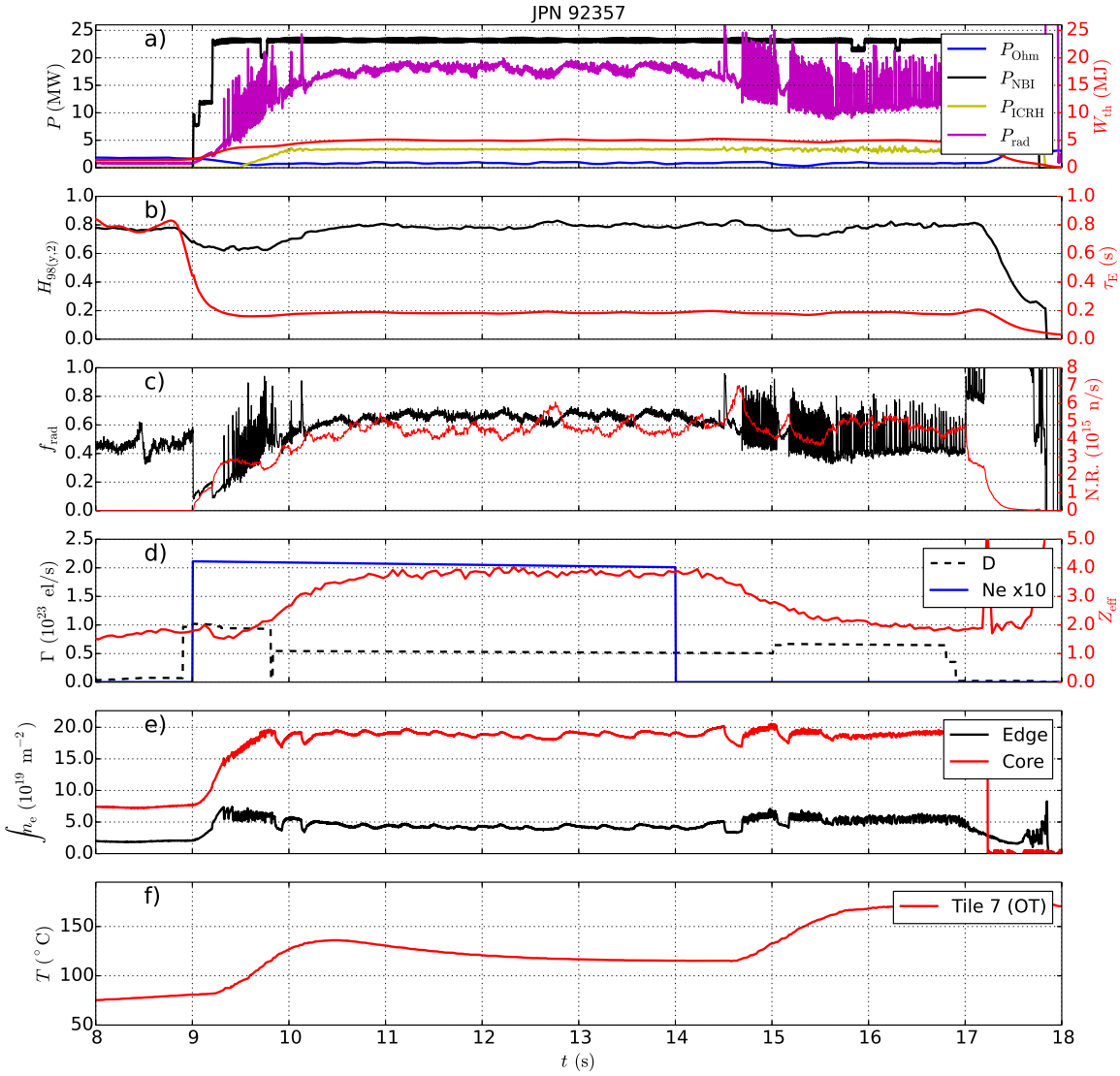

Figure 12. *Timetraces of JPN 92357, a high power discharge ($P_{heat} = 29$ MW) with strong neon seeding. Quantities as described in Fig. 3. The neon puff starts at $t = 9.0$ s, leading to a transition to M-mode at $t = 10.2$ s where the plasma remains until after the end of the neon puff (at $t = 14.0$ s).*

increases, which could not be observed in the discharges discussed above. After the end of the neon puff this central radiation gradually disappears. At a core temperature of about 5 keV Neon can be excluded as cause for this increased core radiation. As shown later in section 4 the tungsten concentration is decreased during the neon seeding and can therefore be excluded as radiator as well. It is possible that the increased core radiation is an artefact from the tomographic reconstruction.

With neon seeding the n_e profile is degraded at the pedestal top while in the core it

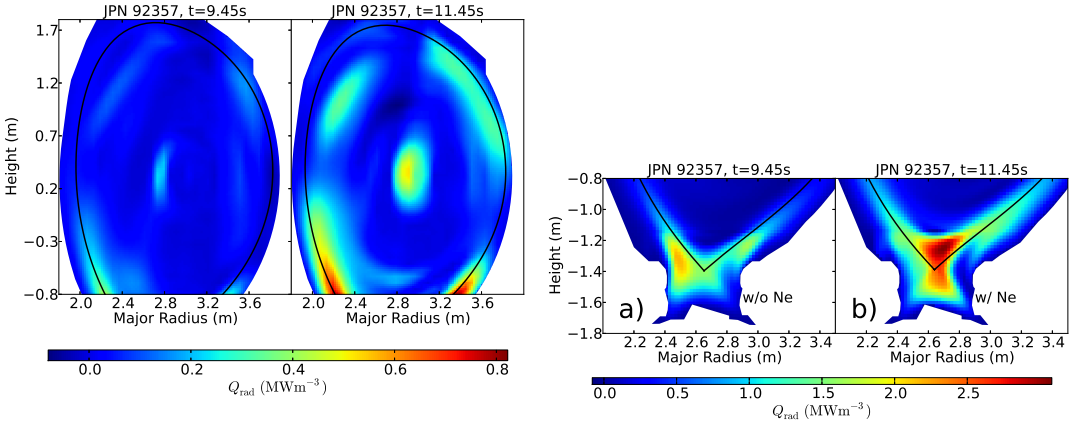

Figure 13. *Core (left) and divertor view (right) of tomographic reconstructions of bolometer data of a) an unseeded and b) a neon seeded phase of JPN 92357 ($P_{\mathrm{heat}} = 29\,\mathrm{MW}$; note the different colour scales). With neon puffing the region with highest radiation power density shifts from the HFS into the confined region close to the X-point. With neon seeding increased radiation in the central core is observed, but it is unclear which effect causes it or if it is an artefact of the tomographic reconstruction.*

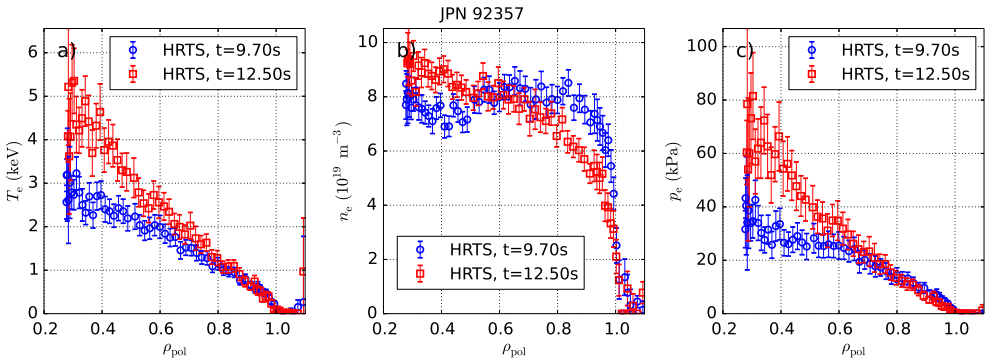

Figure 14. *Median radial profiles of JPN 92357 ($P_{\mathrm{heat}} = 29\,\mathrm{MW}$). The description and observations are similar as in Fig. 4.*

remains unchanged. T_{e} is increased in the core (see Fig. 14). Despite these significant changes the profiles undergo with neon seeding, the energy confinement time remains constant. The thermocouples at the outer target (no data is available for the inner target) measure an increase in temperature between 35 and 55 °C, peaking at $t = 10.0\,\mathrm{s}$, shortly after the beginning of the neon puff, and then decreasing until after the end of the neon puff where it starts to rise again. The targets are complete detached (see Fig. 15). The temperature drops below the sensitivity level of the Langmuir probes of about 5 eV at the outer target with neon seeding, at the inner target these low temperatures are already measured earlier. The ion saturation current is increased at the outer target and an increase can be observed also at the inner target close to the strike point position.

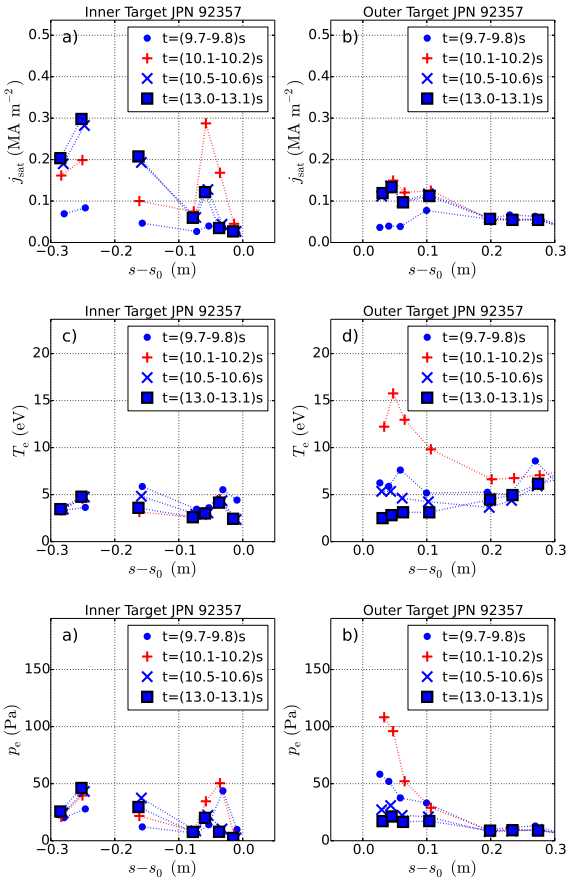

Figure 15. *Time-averaged (median) target profiles of JPN 92357 ($P_{\text{heat}} = 29\,\text{MW}$) as in Fig. 6. In L-mode phases (red) the targets are attached while in H-mode (blue) they are in complete detachment. At the inner target one LP at $s - s_0 \approx -0.2$ was broken and seems to have influenced adjacent probes.*

Both increases are small compared to the ion saturation current measured during an L-mode phase during ramp-up. For positions further from the strike point position at the inner target no statement about the ion saturation current can be made because a broken Langmuir probe at $s - s_0 \approx -0.2$ seems to have affected the measurements of adjacent probes.

2.4. Influence of the Neon Puff on the L-H Transition

In the previous sections the influence of the heating power on the stability of the discharges at strong neon seeding was shown: at $P_{\mathrm{heat}} = 15\,\mathrm{MW}$ the discharge transits back to L-mode with the onset of neon puffing, at $P_{\mathrm{heat}} = 19\,\mathrm{MW}$ it switches between M-mode and L-mode, and even at $P_{\mathrm{heat}} = 29\,\mathrm{MW}$ the presence of an M-mode indicates the vicinity to the L-H threshold. It has to be noted, though, that the core radiation power in the discharges examined here was significant. Usually the L-H power threshold is estimated by the scaling presented in [42]. As the data used for this scaling were derived from machines with carbon as wall material, it might not be as accurate for devices with metallic walls as is JET-ILW with its tungsten divertor and berillium first wall. In Fig. 16 a scaling derived from JET-ILW data in VT configuration [43] (red points) was used to examine the proximity of the net heating power crossing the separatrix P_{SOL} to the L-H power threshold P_{LH} in several neon seeded high radiation discharges. The scaling for VT configuration was chosen because the divertor configuration in JET has a strong influence on the L-H threshold. Because current L-H scalings are derived from discharges with low f_{rad} (typically below 0.5), their results for discharges with a high radiative power fraction as presented here might be invalid. It can be seen in Fig. 16 that for all heating powers P_{SOL} almost all data points lie between 0.9 and $1.5 \cdot P_{\mathrm{LH}}$, independently of the neon puff rate applied. The results presented here are in agreement with the previous observations of transitions to L-mode, transitions between L-mode and M-mode, and M-mode that implied the proximity of most of the examined discharges to the L-H threshold even at highest heating powers.

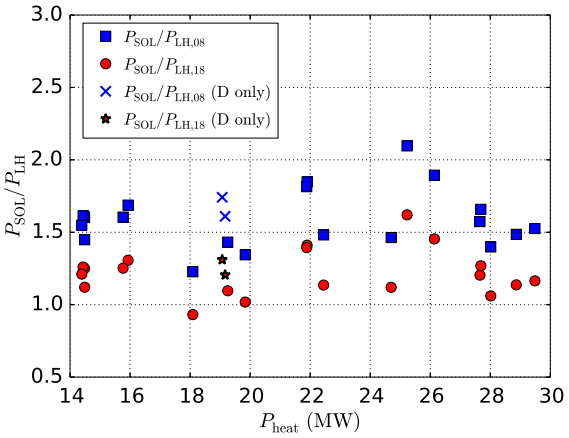

Figure 16. *Power transported in the scrape-off layer* $P_{\mathrm{SOL}} = P_{\mathrm{heat}} - P_{\mathrm{rad,sep}}$ *(*$P_{\mathrm{rad,sep}}$ *being the radiation power from inside the separatrix, hence including the X-point radiator) compared to the L-H threshold powers* $P_{\mathrm{LH,08}}$ *[42] (blue) and* $P_{\mathrm{LH,18}}$ *[43] (red; scaling for JET-ILW in VT configuration) as function of total heating power* P_{heat}*. For most heating powers* P_{SOL} *exceeds* P_{LH} *only by up to* 50 %*. Only at highest heating powers* P_{SOL} *is significantly higher than* P_{LH}*.*

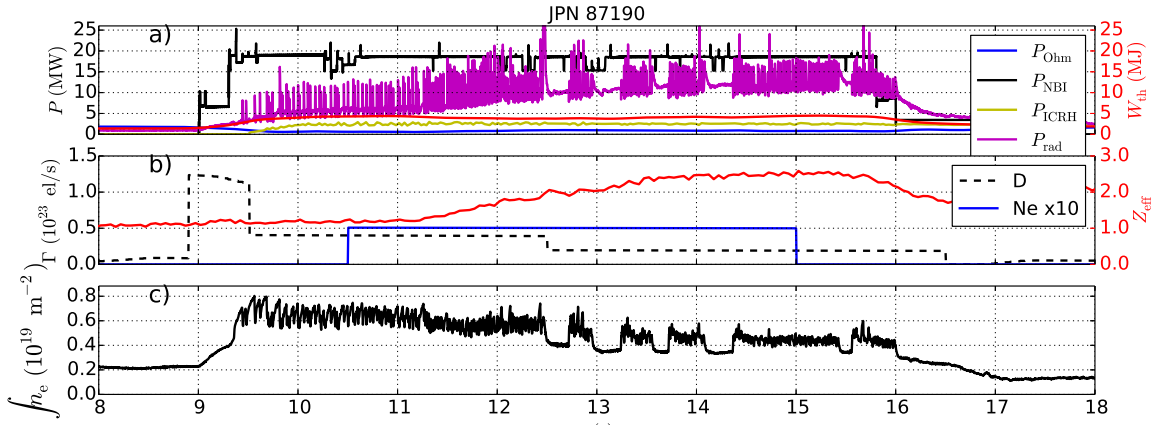

Figure 17. *Timetraces of JPN 87190, a medium heated discharge (P_{heat} = 22 MW) with medium neon seeding. Quantities as described in Fig. 3.*

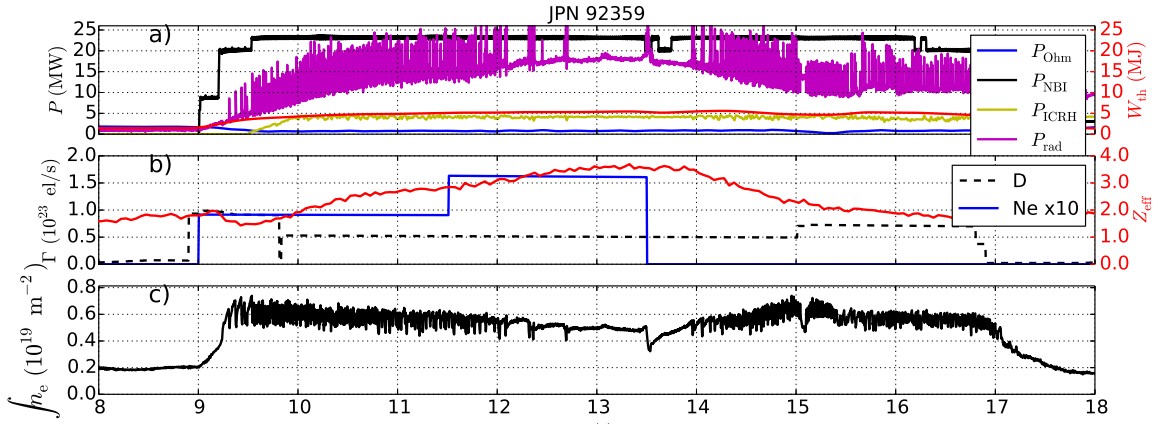

Figure 18. *Timetraces of JPN 92359, a high heated discharge (P_{heat} = 29 MW) with medium neon seeding. Quantities as described in Fig. 3.*

Although the heating power plays a major role for the characteristics observed in the discharges presented above, at a fixed heating power the plasma regime also strongly depends on the neon seeding level. JPN 87190 has a similar heating power (22 MW) as JPN 85443 but a neon puff rate of only about 50 % of this discharge (compare Figs. 7 and 17). In this less seeded discharge the plasma does not permanently enter the M-mode but mostly stays in ELMy H-mode. In contrast to the previously presented discharge JPN 92357 ($\Gamma_{\mathrm{Ne}} = 2.0 \cdot 10^{22}$ el/s, see Fig. 12), at high heating power ($P_{\mathrm{heat}} = 29$ MW) the plasma in JPN 92359 (see Fig. 18) is not in an M-mode but in an ELMy H-mode with the first step of neon seeding ($\Gamma_{\mathrm{Ne}} = 0.9 \cdot 10^{22}$ el/s). An increase of the neon puff rate at $t = 11.5$ s to $\Gamma_{\mathrm{Ne}} = 1.6 \cdot 10^{22}$ el/s leads to a transition to an M-mode regime with back-transitions to L-mode.

Figure 19 shows the fraction of radiated power as a function of the neon seeding rate in several high radiation discharges. With increased neon seeding the radiative

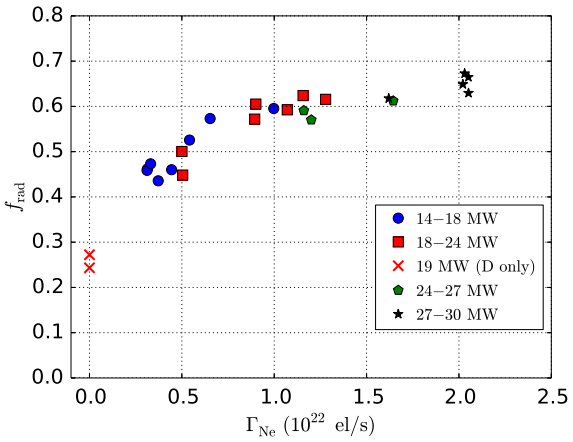

Figure 19. *Radiated power fraction f_{rad} as function of the neon puff Γ_{Ne}. For puff strengths up to $\Gamma_{Ne} \approx 1.0 \cdot 10^{22}$ el/s the radiation is increased with increasing neon puff, for higher puff strengths the curve is in quasi-saturation. By increasing the neon puff, only minor increases in radiation can be achieved. The low f_{rad} even with completely detached targets are yet to determine [17, 18].*

power fraction f_{rad} increases, until a neon puff rate of $\Gamma_{Ne} \approx 1.0 \cdot 10^{22}$ el/s is reached where f_{rad} seems to saturate at values of $f_{rad} = 0.6$. A further increase of the neon puff rate over $2.0 \cdot 10^{22}$ el/s leads only to a small increase in the radiative power fraction up to $f_{rad} = 0.66$. It is noticeable that the discharges found here are all in M-mode regime, without transitions to L-mode. In general, to permanently stay in this regime a high neon seeding rate of $\Gamma_{Ne} > 1.0 \cdot 10^{22}$ el/s and a high heating power over 25 MW were necessary. All examined discharges in this M-mode without transitions to L-mode have a core radiation power $P_{rad,core}$ of over 10 MW. The highest values of f_{rad} could only be reached with a neon puff rate of $\Gamma_{Ne} > 2.0 \cdot 10^{22}$ el/s, though. Since the difference in terms of f_{rad} between discharges with $\Gamma_{Ne} = 1.0 - 2.0 \cdot 10^{22}$ el/s and such with $\Gamma_{Ne} > 2.0 \cdot 10^{22}$ el/s is quite small (see Fig. 19), the radiative power fraction does not seem to play a role in the transition to a stable M-mode without transitions to L-mode, another plasma property affected by the neon puff might contribute to the suppression of transitions to L-mode.

3. Improved Core Energy Confinement

3.1. ASTRA-TGLF Transport Prediction of Core Temperature Profiles

To examine the increase of core temperature and the slight increase of the energy confinement time (see Fig. 3, 7, and 12) in all neon seeded phases, a time point from the unseeded reference discharge JPN 84884 as well as one from the neon seeded discharge JPN 85443 at medium heating power ($P_{heat} = 19$ MW) have been simulated with the ASTRA-TGLF [44, 45, 46, 47] transport code. The dots in Fig. 20 indicate the experimental data. Those in grey areas (i.e. the full n_e profile and the T_i profile for

$\rho_{\mathrm{tor}} > 0.75$) were used as prescribed input of the simulations. $T_{\mathrm{i}} = T_{\mathrm{e}}$ was assumed. The total NBI heating power in both discharges was similar. Since it has been observed in the experiment that due to the lower edge density the NBI penetrates further into the plasma, the radial NBI heating profiles (see Fig. 21) were considered in the simulations. The radiation strongly increases in the edge with neon seeding and was hence included in the simulations as well. Assuming that neon was the only impurity species, the neon content in the seeded case was estimated from Z_{eff}, resulting in a uniform concentration of around 1.3 %. The core temperatures were predicted using the TGLF transport model. The solid lines indicate the simulation results derived from these data. The simulated electron temperatures reproduce the $T_{\mathrm{e/i}}$ increase seen in the experimental profiles. A third dashed line shows the result of a simulation similar to the one of the neon seeded time point with the only difference being that the neon species has been removed from the simulation. This means that $n_{\mathrm{i}} = n_{\mathrm{e}}$. All other quantities, including the n_{e}, $T_{\mathrm{e/i}}$ (for $\rho_{\mathrm{tor}} > 0.75$), Q_{rad} and Q_{NBI} profiles, and Z_{eff} remained as given by the neon seeded experimental data.

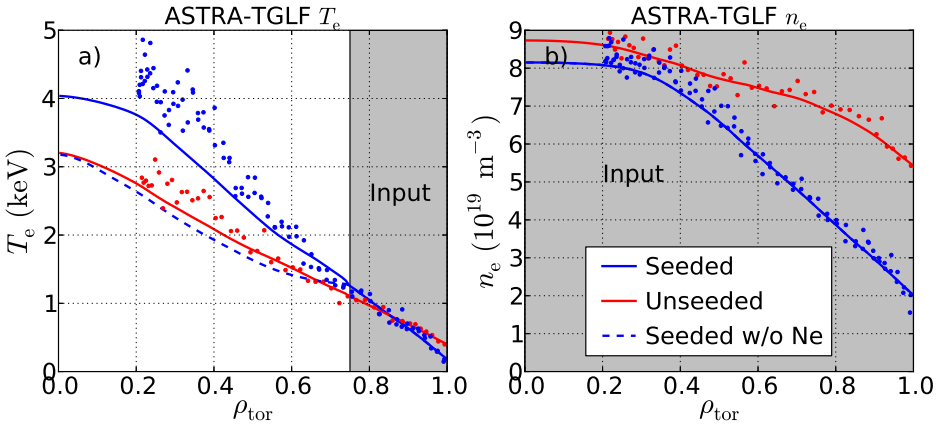

Figure 20. *Experimental electron density and temperature data (dots) of a neon seeded (blue, JPN 85443, $t = 12.8\,\mathrm{s}$) and an unseeded (red, JPN 84884, $t = 13.0\,\mathrm{s}$) discharge, compared to ASTRA-TGLF simulation results (solid lines) based on the experimental data in the grey areas. The dashed line marks the results of a simulation of the neon seeded time point with the neon species removed from the simulation while all other parameters were kept constant.*

When in simulations based on profiles for the seeded phase (solid blue line in Fig. 20) neon is removed (dashed blue line), the temperature drops below the values from the simulation of the unseeded phase (red line). This shows that effects introduced by the impurity other than radiation are responsible for the core confinement improvement. The ASTRA-TGLF simulations suggest that a dilution of the main ion density by the neon impurity reduced the edge ion pressure gradient and thus stabilises the ion temperature gradient (ITG) mode. The ITG turbulence is driven by the majority ion species (D) at the most unstable wavenumber. Due to the addition of neon, the

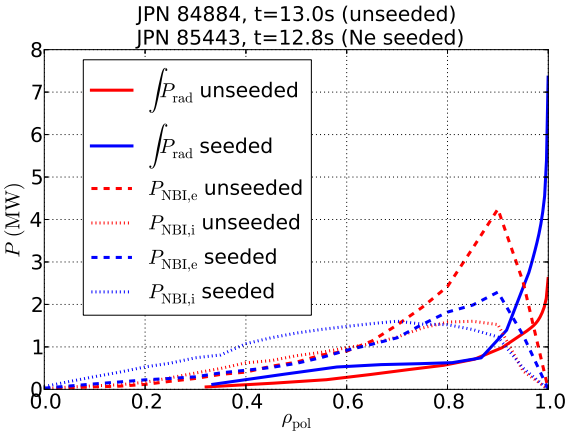

Figure 21. *Radial profiles of deposited power by the NBI heating (dashed and dotted lines) and radially integrated radiation (solid lines) for time points with (blue) and without (red) neon seeded. Due to lower edge density, the NBI deposition is shifted towards the core when neon is seeded. The radiation at* $\rho_{\mathrm{pol}} > 0.9$ *is significantly increased with neon seeding.*

deuterium concentration decreases with respect to the electron density, which pushes the turbulence from the ITG towards the electron drift wave that is stable due to the high collisionality. Hence, the ITG turbulence decreases in amplitude and the ion heat diffusivity is reduced, allowing T_{i} to increase. This so-called "dilution" effect is valid until neon becomes the majority species. Since ITG turbulence is driven by the ion temperature gradient, the reduction in density gradient, which acts as a passive element, is not relevant for this process. This stabilisation of ITG modes leads to increased core temperatures and therefore to an improved core energy confinement [48, 49]. The effect of increased confinement observed in the core is to distinguish from a potentially counter-acting effect in the pedestal region where the increased radiation might lead to diminished confinement. In fact, the overall confinement time remains nearly constant, suggesting an effect opposed to the core confinement improvement. In other JET discharges with neon seeding rates in the range $1–5{\cdot}10^{23}$ el/s it was also found that the neon seeding had no effect on the confinement (but on the fusion performance due to increasing density and decreasing temperature) [11]. A doping effect (i.e. that the neon affects the plasma beyond the displacement of deuterium), as described in [50], was observed in these low neon seeded discharges. This effect could not be observed in the high seeded discharges presented in this article which might be attributed to their lower Z_{eff} level.

3.2. Density Peaking

In another study of neon seeded JET discharges at significantly lower neon seeding rates a peaking of the electron density [50, 51], i.e. an increase of the ratio of core to pedestal

density, $n_{\mathrm{e,core}}/n_{\mathrm{e,ped}}$ (with the core position at $\rho_{\mathrm{pol}} = 0.25$), was observed while the volume averaged density was decreased [11]. This was caused by an inward particle pinch. In our experiments with higher neon seeding rates a density peaking could be observed as well (see Fig. 22). In Fig. 22 the core and pedestal top electron densities relative to the line-averaged electron density $\bar{n}_{\mathrm{e}}$ are shown. Due to the degradation of the pedestal and hence the absence of a proper pedestal top position, the pedestal top position was taken from the unseeded reference discharge, at $R_{\mathrm{n,ped}} = 3.79\,\mathrm{m}$; the core density was measured at $R_{\mathrm{n,core}} = 3.30\,\mathrm{m}$. It is clearly visible that with increased neon puffing rate the relative core density remains constant while only the relative pedestal top density decreases. The density peaking can therefore be attributed to a density decrease in the pedestal region rather than an increase in the core. The reason for the degraded pedestal density has yet to be investigated.

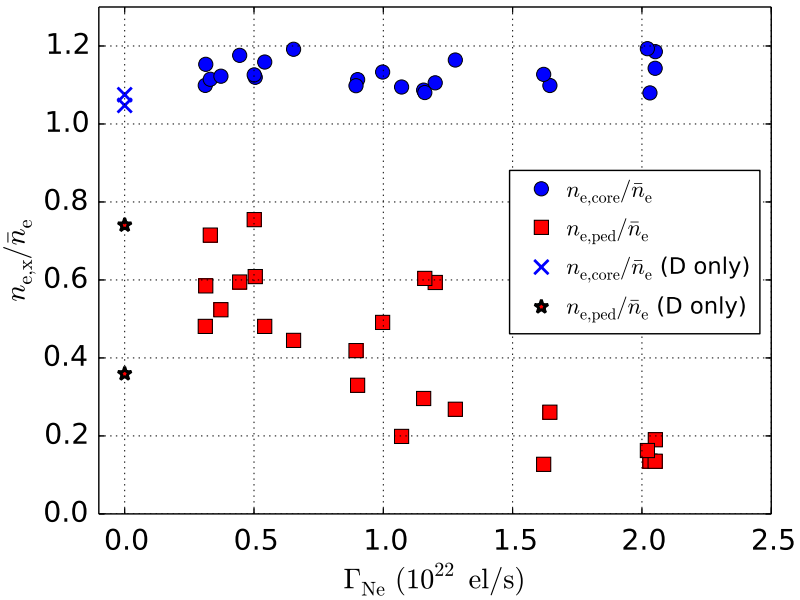

Figure 22. *Electron density in core (blue, measured at $R = 3.30\,\mathrm{m}$) and pedestal top (red, measured at $R = 3.79\,\mathrm{m}$) relative to the line-averaged density $\overline{n_{\mathrm{e}}}$. Due to the degraded pedestal the pedestal top position was defined by the pedestal top position of an unseeded reference discharge. The neon puffing seems to affect only the pedestal region.*

With a decreasing pedestal top density and a nearly constant pedestal top temperature the pedestal top pressure is decreasing as well. It can be observed, though, that $H_{98(\mathrm{y},2)}$ does not correlate with the pedestal top pressure (see Fig. 23). Thus, the decrease of the pedestal top pressure does not affect the global energy confinement time. Instead, the effect of more stable ITG modes in the core was shown to be the dominating influence on the confinement.

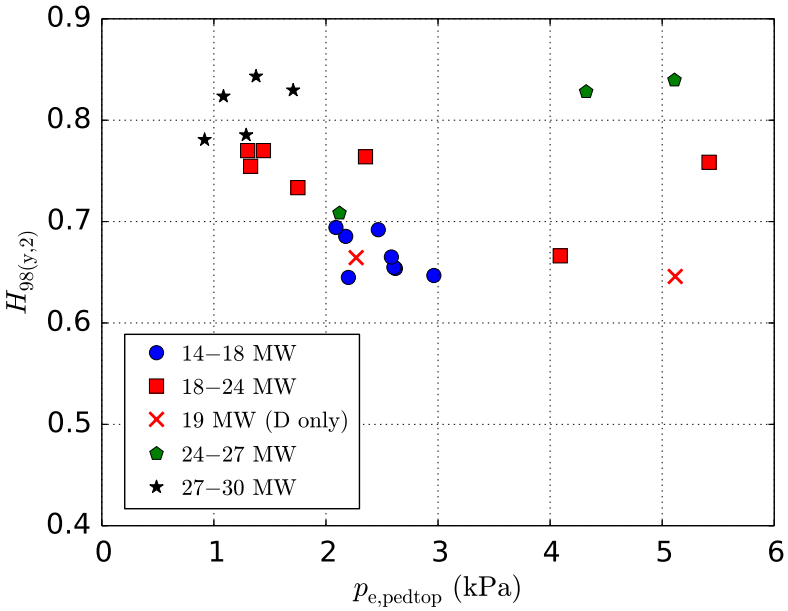

Figure 23. *$H_{98(y,2)}$ as function of pedestal top pressure p_{pedtop}. A correlation can not be found. It is worth noting that the lowest heated discharges gather at similar pedestal top pressures while higher heated discharges exhibit a wider range of pedestal top pressures.*

3.3. Energy Confinement

With respect to future fusion devices the effect of neon seeding on the energy confinement has to be studied. In Fig. 24 the confinement factor $H_{98(y,2)}$ versus the normalised plasma $\beta_N = 2\mu_0 p/B^2$ ratio is shown. For ITER, at $\beta_N = 1.8$ an $H_{98(y,2)}$ of 1.0 is required to reach the scientific goals of $Q = 10$ [52]. In the present discharges a maximum value of only $H_{98(y,2)} = 0.85$ was reached at highest heating powers. It has to be considered, though, that the unseeded discharges have already a low $H_{98(y,2)}$ value. As it was shown in the previous sections, neither the energy confinement time τ_E nor the confinement factor $H_{98(y,2)}$ change significantly with the onset of the neon puff. However, it has already been found that the vertical target configuration leads to lower confinement than the corner configuration [13, 14] and that high D_2 puffs decrease the confinement as well [13, 30, 31]. Thus, the cause for the low $H_{98(y,2)}$ lies rather in the target configuration and in the high D_2 puffs than in the neon puff.

3.4. Neutron Rate

In present-day machines like JET the neutrons are primarily created by the interaction of the NBI deuterons with the thermal deuterons (so-called beam-target reactions) rather than by the interaction of thermal deuterons amongst each other. In Fig. 25 it is shown how the neutron rate increases with increased neon puffing. The dependence on the heating power is less pronounced. The result shown here is in contrast to [11, 50, 51],

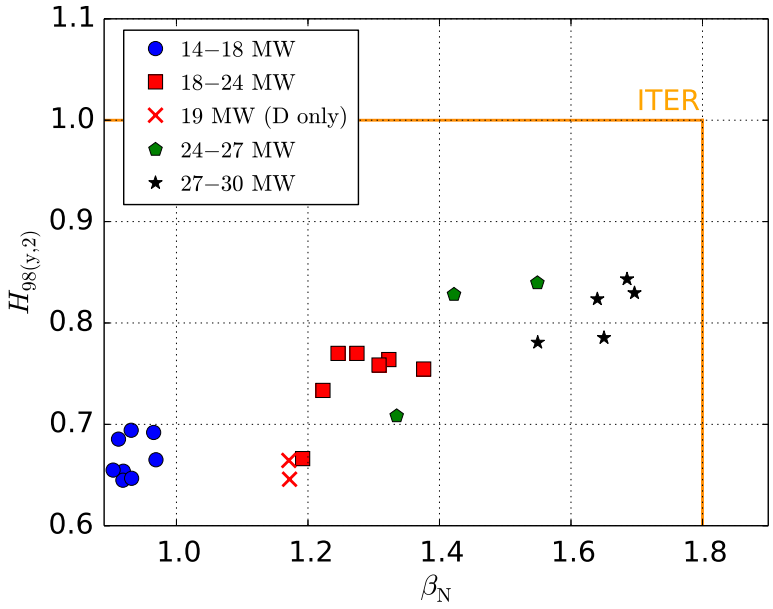

Figure 24. *$H_{98(y,2)}$ as function of β_N. The ITER target value of $H_{98(y,2)} = 1.0$ at $\beta_N = 1.8$ [52] could not be met with the neon seeded discharges. The unseeded discharges have equally low values due to the high deuterium puff.*

where a decrease of the neutron rate from $4.5 \cdot 10^{15}$ n/s to $2.5 \cdot 10^{15}$ n/s has been observed at a puff strength of $\Gamma_{Ne} = 2 \cdot 10^{21}$ el/s [50, 51]. This is explained by the authors with a decrease in the core ion temperature. In the experiments presented in this article the opposite is observed: an increased core ion temperature and an increased neutron rate. Further reasons for the increase of the neutron rate in the highly neon seeded discharges are yet to investigate. It is possible that the deeper penetration of the NBI beams in the plasma due to the degraded pedestal density (while the core density remains constant and the ion temperature increases) might have an impact on the neutron rate, e.g. due to a better confinement and increased slowing down time of the fast beam particles.

4. Impurity Content

The core impurity concentration in fusion plasmas is to be kept as low as possible. The deteriorating effect of an impurity depends mainly on its charge state [6]. E.g., the maximum permitted tungsten concentration is in the order of some 10^{-5}. Since seeded impurities could increase the sputtering of wall material the influence of neon seeding on the concentrations of typical wall materials are studied. A recently developed method allows to self-consistently calculate the composition of JET-ILW plasmas including multiple impurity species [53, 54]. The different impurities are included in the analysis in a step-wise approach gradually increasing the analysis complexity in the search for the best match to all the available diagnostic measurements. For the cases reported here four elements (Be, Ne, Ni, W) were necessary to match simultaneously the observed

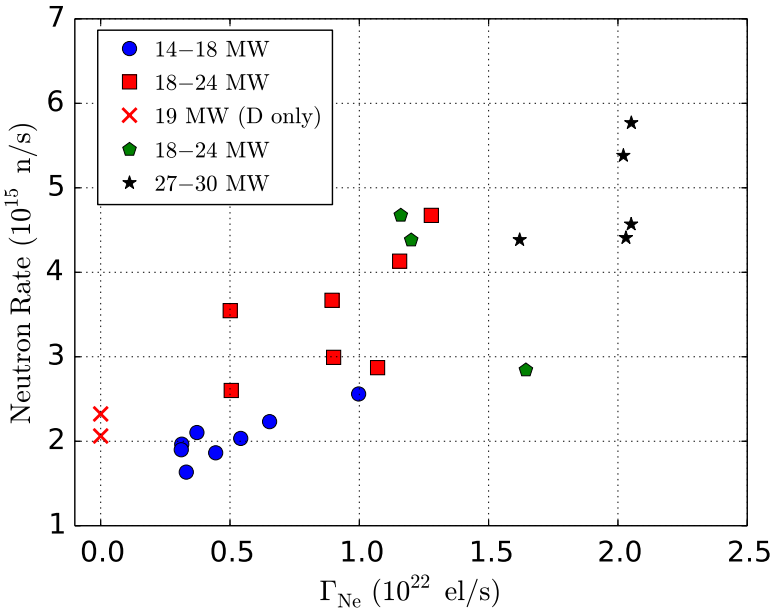

Figure 25. *Neutron rate as function of the neon seeding rate* Γ_{Ne}*. An increase of the neutron rate with increased neon seeding can be seen.*

soft X-ray emission, the W concentration measured by passive vacuum-ultra-violet spectroscopy, the line-of-sight integrated measurement of the effective charge Z_{eff}, the observed poloidal asymmetry of the SXR emission and the line-of-sight integrals of the total radiation as measured by bolometry. Beryllium is taken as a constant background originating from the main chamber walls. Neon is left free to evolve in time to match the measured effective charge. Tungsten is calculated directly from the observed SXR emission subtracting the contributions from all other radiating elements. The inclusion of nickel is necessary to obtain a satisfactory match with the total radiated power as measured by the bolometer and is modelled from the initial estimate of the W density using theory-driven assumptions [54].

The results of this analysis are shown in Fig. 26 for JPN 92357. It is observed that after the end of the neon puff at $t = 14.0\,\mathrm{s}$ the tungsten density increases slightly, implying that the detached divertor diminished the tungsten sputtering despite the increased sputtering potential of neon. This observation is verified by the W I signal of the visible light spectroscopy in the inner divertor that demonstrates an equal or reduced gross tungsten erosion in the three neon seeded pulses presented in section 2 compared to the unseeded reference pulse JPN 84884. Since in the analysis method the nickel density distribution is based on the tungsten density distribution the trends for nickel are the same. In JPN 87195 (similar to JPN 87196 presented above) with the onset of the neon seeding the nickel and the tungsten concentrations decrease. The tungsten concentration in JPN 85443 demonstrates a contrary behaviour: after the beginning of the neon seeding tungsten concentration increases. An increase of these concentrations

during the starting phase of the discharge was observed also in JPN 87195, but in JPN 85443 the concentrations do not decrease when the neon is puffed. This might be attributed to the HLH-transitions which are not present in the other two discharges.

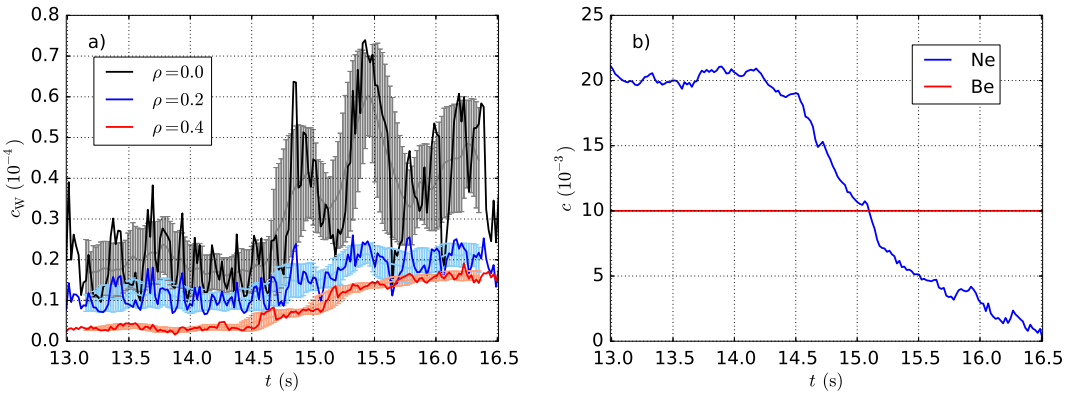

Figure 26. *Results of the impurity content analysis [53, 54] for JPN 92357. a) Time evolution of the tungsten concentration* c_W *at three different radial positions. The light-coloured lines and errorbars exhibit the moving average mean and standard deviation (window size:* 320 ms*). After the end of the neon puff at* $t = 14.0$ s c_W *increases. Since the nickel concentration depends on the tungsten concentration in the analysis, it exhibits the same trend. b) Time evolution of the neon concentration (fixed in radius) and the beryllium concentration (fixed in radius and time).*

As a measure for the generalised impurity concentration of the plasma, Z_{eff} can be studied. Figure 27 shows that with increased neon seeding also Z_{eff} increases. This seems conflicting with the increase of the neutron rate with increased neon seeding because an increased impurity content leads to a dilution of the plasma and to decreased beam-target reactions. A hollow neon density profile as a possible explanation is rather unlikely since the impurity content analysis as well as the ASTRA-TGLF simulations assumed flat neon density profiles and successfully reproduced experimental measurements. There are no spectroscopic measurements of the radial neon distribution yet. As discussed at the end of the previous section, another reason for the increasing neutron rate could lie in the decreased pedestal density which permits a larger fraction of the NBI beam power to be deposited in the core, outweighing the dilution by neon.

5. Poloidal Radiation Distribution

It was shown in Fig. 19 that the radiative power fraction almost saturates when the neon seeding rate is increased above $\Gamma_{\text{Ne}} \approx 1.0 \cdot 10^{22}$ el/s. The distribution of the radiation might change at the highest neon puffing rates, though. Figure 28 shows the radiation powers from the divertor, the core (defined as the region inside $\rho_{\text{pol}} = 0.95$) and the pedestal region ($0.95 < \rho_{\text{pol}} < 1.0$, including also an eventually existing X-point radiator) as function of the neon puff rate. While at low neon puff rates the

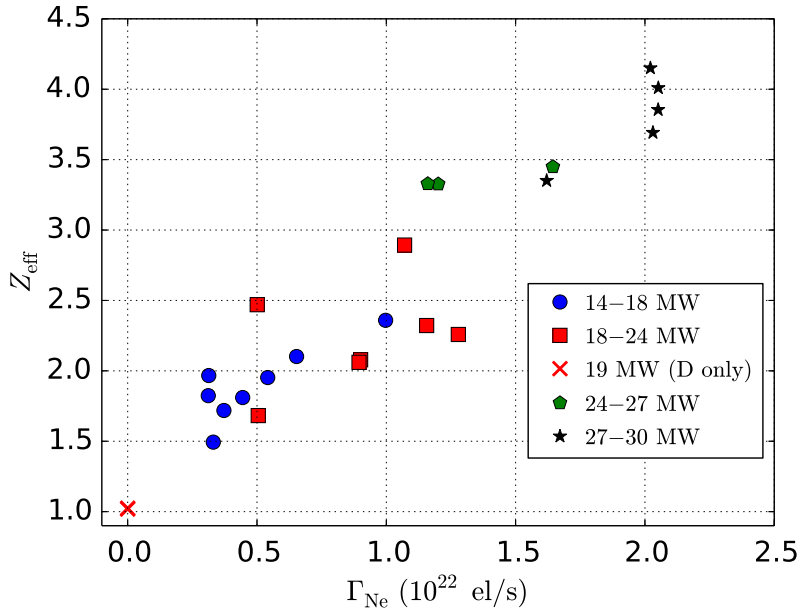

Figure 27. *Line-averaged effective charge state Z_{eff} as function of the neon puff Γ_{Ne}.*

divertor radiation power is similar to the core and the pedestal radiation power (around 2 MW each), the radiation from the core and particularly from the pedestal region are increased up to 6–8 MW with increasing neon seeding. The divertor radiation barely increases (only up to 4 MW), which is in accordance with [10], where a maximum of the divertor radiation power as function of the neon seeding rate has been found.

For the heating power a similar picture can be found: up to a heating power of $P_{\mathrm{heat}} = 24$ MW divertor, pedestal, and core radiation powers are similar, increasing up to 4 MW. With increasing heating powers pedestal and core radiation powers increase further up to around 7 MW while the divertor radiation power decreases to 2 MW. The line-averaged densities of the neon seeded discharges presented in this article are in the same range (around $5–7 \cdot 10^{19}\,\mathrm{m}^{-3}$), thus a density dependence cannot be discriminated. It should be noted, though, that the accuracy of the magnetic equilibrium reconstruction and the spatial resolution of the bolometer system do not permit exact calculations of radiation powers for the single areas – especially in the narrow pedestal region – and that the values presented here can therefore only give indications.

A correlation between the radiation power of the X-point region (defined as the region with $\rho_{\mathrm{pol}} \leq 1.0$ and $z \leq -1.2$ m) and the core radiation power could be observed: With increasing core radiation power the radiation power of the X-point increases approximately linearly. A correlation between the formation of the X-point radiator and the neon seeding rate was not observed. Even though all discharges with neon puff rates $> 0.5 \cdot 10^{22}$ el/s had an X-point radiator, there were also discharges found with lower neon seeding rates and X-point radiator. The density range of the presented

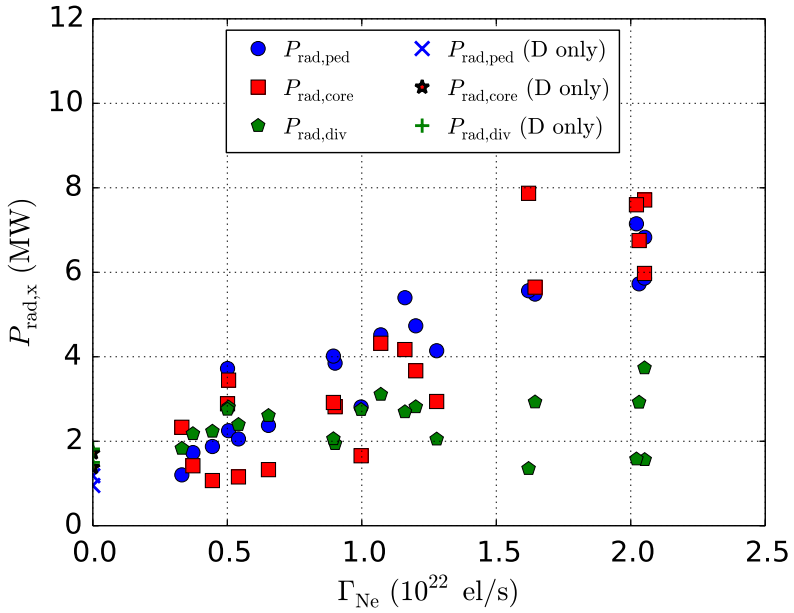

Figure 28. *Radiation powers of divertor, core (inside a roughly estimated pedestal top position, $\rho_{\mathrm{pol}} < 0.95$) and pedestal (between pedestal and separatrix, $\rho_{\mathrm{pol}} < 0.95$) as function of Γ_{Ne}. The radiation is primarily increasing in the pedestal region and in the core (by a factor of 5–6 between the lowest heated and the highest heated discharge), while the radiation power in the divertor increases only by a factor of 3–4.*

discharges was too small to see clear dependencies of the X-point radiator on the line-averaged density, especially at low heating powers. The maximum X-point radiation power is around 1–2 MW. A detailed analysis of the X-point radiator by spectroscopic or numerical means (as shown for ASDEX Upgrade in [55, 56]) are yet to be performed.

In all of the neon seeded discharges examined for this article, it was observed that the appearance of the X-point radiator, the degradation of the pedestal density, and the detachment of both divertor targets are correlated with each other under the following conditions:

(i) The plasma is in stable H-mode or M-mode. During L-mode phases, during LH/HL-transitions, and during the plasma ramp-up phase one or more of the aforementioned phenomena (and therefore their correlation) might not be observed.

(ii) Neon is being puffed. At the beginning of the neon puff, it takes some time (1–1.5s) until the neon takes effect; in this period these phenomena might not be observed. After the end of the neon puff the neon is pumped out and thus, both the X-point radiator and the pedestal degradation are not observed any longer.

In neon seeded discharges with an initial type-I ELMy H-mode phase it is observed that with the formation of the X-point and the degradation of the density pedestal the plasmas undergo a transition from type-I to type-III ELMs. A correlation of the

formation of the X-point radiator with the transition to M-mode was not observed.

6. Discussion and Conclusions

The seeding of impurities is crucial in future fusion devices like DEMO in order to protect the divertor target tiles. In this paper it has been discussed what impact strong neon seeding can have on the core, pedestal, and divertor conditions. In M-mode phases, which are in JET typically found close to the L-H power threshold, the joint appearance of an X-point radiator, a degraded density pedestal, and the detached targets was observed. In L-mode phases it was noted that at least one of the divertor targets was attached, independently of the presence of an X-point radiator. A degradation of the density pedestal could not be seen in L-mode. The detached M-mode phases might not be problematic with regard to future fusion devices, the back-transitions into attached L-mode surely are due to their peak heat load. Only at high heating powers ($P_{\mathrm{heat}} > 25\,\mathrm{MW}$) and high neon puff rates ($\Gamma_{\mathrm{Ne}} > 1.0 \cdot 10^{22}\,\mathrm{el/s}$) the plasma enters an M-mode regime without back-transitions to L-mode. In these discharges the targets are completely detached.

Through ASTRA-TGFL simulations it could be found that neon stabilises the ITG mode in the core due to the dilution effect, leading to higher core temperatures and together with a somewhat degraded pedestal approximately constant energy confinement times. While the core profiles are not negatively affected by neon seeding, in the pedestal a degradation of the electron density is observed. As this coincides with a strong increase of radiation power density in the edge including the X-point region, a correlation between the increased edge radiation and the pedestal density degradation might be possible.

Detachment is characterised by a drop of pressure between the midplane and the target position. Since (compared to core and pedestal radiation) only a small increase of divertor radiation power of maximum 2 MW was observed, it is questionable if an increased divertor radiation leads to the pressure drop in front of the targets. Based on the available data it was experimentally not possible to determine if a degraded pressure profile upstream at the separatrix causes the pressure drop at the targets.

Due to the strong seeding with high radiative power fractions, detached targets, and no loss of energy confinement, the regime found in these experiments seems to be potentially interesting for future fusion devices like ITER or DEMO. Its suitability for such devices has to be further examined. The low energy confinement at unseeded time points are caused by the target configuration and the high deuterium puff and might increase in more favourable target configurations and at lower densities. It should be clarified if in such discharges with higher energy confinement at unseeded time points the trend of a constant or slightly increasing energy confinement with neon seeding can be observed similarly as presented here.

Moreover, to examine a possible extrapolation of the experimental findings to future devices additional numerical modelling is required, e.g. by core transport codes, pedestal stability analysis, or two-dimensional SOL codes. The latter would allow for a joint

analysis of the stability of the X-point radiator, the pedestal density degradation and the detached targets. So far, at JET the EDGE2D-EIRENE simulation of the X-point radiator with nitrogen seeding led to numerical issues [16]. At ASDEX Upgrade, the X-point radiator could be reproduced with SOLPS modelling with nitrogen seeded [55]. To validate the simulations against the observations of the pulses presented here (and hence to numerically reproduce them) would not only allow to analyse them in more detail (e.g. to possibly clarify if complete detachment with neon seeding was only possible with a loss of upstream separatrix pressure) but also to extrapolate the simulations to larger devices.

Even though the dilution of the main ion species with neon leads to a beneficial stabilisation of the ITG mode in the core and to a decreasing tungsten concentration, especially in the core, the neon itself might also enrich in the plasma core. Further spectroscopic measurements are required to tackle this question. This might determine if the flushing effect of ELMs is required.

Acknowledgments

This work has been carried out within the framework of the EUROfusion Consortium and has received funding from the Euratom research and training programme 2014-2018 and 2019-2020 under grant agreement No 633053. The views and opinions expressed herein do not necessarily reflect those of the European Commission.

References

[1] Wenninger R P, Bernert M, Eich T, Fable E, Federici G, Kallenbach A, Loarte A, Lowry C, McDonald D, Neu R, Pütterich T, Schneider P, Sieglin B, Strohmayer G, Reimold F and Wischmeier M 2014 *Nuclear Fusion* **54** 114003 ISSN 0029-5515

[2] Wischmeier M, The ASDEX Upgrade Team and JET EFDA Contributors 2015 *Journal of Nuclear Materials* **463** 22–29 ISSN 0022-3115

[3] Zohm H, Angioni C, Fable E, Federici G, Gantenbein G, Hartmann T, Lackner K, Poli E, Porte L, Sauter O, Tardini G, Ward D and Wischmeier M 2013 *Nuclear Fusion* **53** 073019 ISSN 0029-5515

[4] Giruzzi G, Artaud J F, Baruzzo M, Bolzonella T, Fable E, Garzotti L, Ivanova-Stanik I, Kemp R, King D B, Schneider M, Stankiewicz R, Stępniewski W, Vincenzi P, Ward D and Zagórski R 2015 *Nuclear Fusion* **55** 073002 ISSN 0029-5515

[5] Pütterich T, Neu R, Dux R, Whiteford A D, O'Mullane M G, Summers H P and The ASDEX Upgrade Team 2010 *Nuclear Fusion* **50** 025012 ISSN 0029-5515

[6] Pütterich T, Fable E, Dux R, O'Mullane M, Neu R and Siccinio M 2019 *Nuclear Fusion* **59** 056013 ISSN 0029-5515

[7] Kallenbach A, Bernert M, Beurskens M, Casali L, Dunne M, Eich T, Giannone L, Herrmann A, Maraschek M, Potzel S, Reimold F, Rohde V, Schweinzer J, Viezzer E, Wischmeier M and The ASDEX Upgrade Team 2015 *Nuclear Fusion* **55** 053026 ISSN 0029-5515

[8] Kallenbach A, Bernert M, Dux R, Casali L, Eich T, Giannone L, Herrmann A, McDermott R, Mlynek A, Müller H W, Reimold F, Schweinzer J, Sertoli M, Tardini G, Treutterer W, Viezzer E, Wenninger R, Wischmeier M and The ASDEX Upgrade Team 2013 *Plasma Physics and Controlled Fusion* **55** 124041 ISSN 0741-3335

[9] Bernert M, Wischmeier M, Huber A, Reimold F, Lipschultz B, Lowry C, Brezinsek S, Dux R, Eich

T, Kallenbach A, Lebschy A, Maggi C, McDermott R, Pütterich T, Wiesen S, JET Contributors, The EUROfusion MST1 Team and The ASDEX Upgrade Team 2017 *Nuclear Materials and Energy* **12** 111–118 ISSN 2352-1791

[10] Huber A, Wischmeier M, Lowry C G, Brezinsek S, Maggi C F, Reinke M L, Sergienko G, Aho-Mantila L, Arnoux G, Beurskens M N A, Clever M, Devaux S, Esser H G, Giroud C, Groth M, Jachmich S, Järvinen A, Linsmeier C, Lipschultz B, Matthews G F, Maddison G, Marsen S, Meigs A G, Mertens P, Nave M F F, Philipps V, Stamp M, Wiesen S and JET-EFDA Contributors 2014 Impact of strong impurity seeding on the radiation losses in JET with ITER-like wall *Proceedings of the 41th EPS Conference on Controlled Fusion and Plasma Physics, Berlin, 2014* P1.031 URL `http://ocs.ciemat.es/EPS2014PAP/pdf/P1.031.pdf`

[11] Challis C D, Belonohy E, Czarnecka A, Frigione D, Giroud C, Graves J, Hobirk J, Huber A, Joffrin E, Krawczyk N, Lawson K, Mantsinen M, McClements K, O'Gorman T, Silburn S, Sips A, Solano E and JET Contributors 2017 Impact of neon seeding on fusion performance in JET ILW hybrid plasmas *Proceedings of the 44th EPS Conference on Controlled Fusion and Plasma Physics, Belfast, 2017* P2.153 URL `http://ocs.ciemat.es/EPS2017PAP/pdf/P2.153.pdf`

[12] Giroud C, Maddison G, McCormick K, Beurskens M N A, Brezinsek S, Devaux S, Eich T, Frassinetti L, Fundamenski W, Groth M, Huber A, Jachmich S, Järvinen A, Kallenbach A, Krieger K, Moulton D, Saarelma S, Thomsen H, Wiesen S, Alonso A, Alper B, Arnoux G, Belo P, Boboc A, Brett A, Brix M, Coffey I, de la Luna E, Dodt D, Vries P D, Felton R, Giovanozzi E, Harling J, Harting D, Hawkes N, Hobirk J, Jenkins I, Joffrin E, Kempenaars M, Lehnen M, Loarer T, Lomas P, Mailloux J, McDonald D, Meigs A, Morgan P, Nunes I, van Thun C P, Riccardo V, Rimini F, Sirinnelli A, Stamp M, Voitsekhovitch I and JET EFDA Contributors 2012 *Nuclear Fusion* **52** 063022 ISSN 0029-5515

[13] Maggi C F, Saarelma S, Casson F J, Challis C, de la Luna E, Frassinetti L, Giroud C, Joffrin E, Simpson J, Beurskens M, Chapman I, Hobirk J, Leyland M, Lomas P, Lowry C, Nunes I, Rimini F, Sips A C C, Urano H and JET Contributors 2015 *Nuclear Fusion* **55** 113031 ISSN 0029-5515

[14] Joffrin E, Tamain P, Belonohy E, Bufferand H, Buratti P, Challis C D, Delabie E, Drewelow P, Dodt D, Frassinetti L, Garcia J, Giroud C, Groth M, Hobirk J, Jarvinen A E, Kim H T, Koechl F, Kruezi U, Lipschutz B, Lomas P J, de la Luna E, Loarer T, Maget P, Maggi C, Matthews G, Maviglia F, Meigs A, Nunes I, Pucella G, Rimini F, Saarelma S, Solano E, Sips A C C, Tsalas M, Voitsekhovitch I, Weisen H and the JET Contributors 2017 *Nuclear Fusion* **57** 086025 ISSN 0029-5515

[15] Loarte A 2001 *Plasma Physics and Controlled Fusion* **43** R183–R224 ISSN 0741-3335

[16] Jaervinen A E, Brezinsek S, Giroud C, Groth M, Guillemaut C, Belo P, Brix M, Corrigan G, Drewelow P, Harting D, Huber A, Lawson K D, Lipschultz B, Maggi C F, Matthews G F, Meigs A G, Moulton D, Stamp M F, Wiesen S and JET Contributors 2016 *Plasma Physics and Controlled Fusion* **58** 045011 ISSN 0741-3335

[17] Matthews G F, Bunting P, Devaux S, Drewelow P, Guillemaut C, King D B, Lerche E, Silburn S, Szepesi G, Riccardo V, Thompson V and JET Contributors 2017 *Nuclear Materials and Energy* **12** 227–233 ISSN 2352-1791

[18] Guillemaut C, Drewelow P, Matthews G F, Kukushkin A S, Pitts R A, Abreu P, Brezinsek S, Brix M, Carman P, Coelho R, Devaux S, Flanagan J, Giroud C, Harting D, Lowry C G, Maggi C F, Militello F, Perez von Thun C, Solano E R, Widdowson A, Wiesen S, Wischmeier M, Wood D and JET Contributors 2017 *Nuclear Materials and Energy* **12** 234–240 ISSN 2352-1791

[19] Pasqualotto R, Nielsen P, Gowers C, Beurskens M, Kempenaars M, Carlstrom T, Johnson D and JET-EFDA Contributors 2004 *Review of Scientific Instruments* **75** 3891–3893 ISSN 0034-6748

[20] Frassinetti L, Beurskens M N A, Scannell R, Osborne T H, Flanagan J, Kempenaars M, Maslov M, Pasqualotto R, Walsh M and JET-EFDA Contributors 2012 *Review of Scientific Instruments* **83** 013506 ISSN 0034-6748

[21] Stangeby P C 2000 *The Plasma Boundary of Magnetic Fusion Devices* (IOP Publishing)

[22] Sun H J, Wolfrum E, Kurzan B, Eich T, Lackner K, Scarabosio A, Pérez I P, Kardaun O, Faitsch

M, Potzel S, Stroth U and the ASDEX Upgrade Team 2017 *Plasma Physics and Controlled Fusion* **59** 105010 ISSN 0741-3335

[23] de la Luna E, Sánchez J, Tribaldos V, contributors J E, Conway G, Suttrop W, Fessey J, Prentice R, Gowers C, Chareau J M and JET-EFDA Contributors 2004 *Review of Scientific Instruments* **75** 3831–3833 ISSN 0034-6748

[24] Kadota K, Otsuka M and Fujita J 1980 *Nuclear Fusion* **20** 209–212 ISSN 0029-5515

[25] Fuchs J C, Mast K F, Hermann A, Lackner K and ASDEX-Upgrade-, NBI- and ICRH-Teams 1994 Twodimensional reconstruction of the radiation power density in ASDEX upgrade *Proceedings of the 21st EPS Conference on Controlled Fusion and Plasma Physics, Montpellier, 1994* vol Vol 18B pp 1308–1311

[26] Ingesson L, Reichle R, Fehmers G, Guo H, Lauro-Taroni L, Loarte A and Simonini R 1997 Radiation distribution and neutral-particle loss in the JET MkI and MkIIA divertors *Proceedings of the 24th EPS Conference on Controlled Fusion and Plasma Physics, Berchtesgaden, 1997* vol Vol 21A pp 113–116

[27] Ingesson L C, Alper B, Chen H, Edwards A W, Fehmers G C, Fuchs J C, Giannella R, Gill R D, Lauro-Taroni L and Romanelli M 1998 *Nuclear Fusion* **38** 1675–1694 ISSN 0029-5515

[28] Boboc A, Gil C, Pastor P, Spuig P, Edlington T, Dorling S and JET-EFDA Contributors 2012 *Review of Scientific Instruments* **83** 10E341 ISSN 0034-6748

[29] ITER Physics Expert Group on Confinement and Transport, ITER Physics Expert Group on Confinement Modelling and Database and ITER Physics Basis Editors 1999 *Nuclear Fusion* **39** 2175–2249 ISSN 0029-5515

[30] Joffrin E, Baruzzo M, Beurskens M, Bourdelle C, Brezinsek S, Bucalossi J, Buratti P, Calabro G, Challis C D, Clever M, Coenen J, Delabie E, Dux R, Lomas P, de la Luna E, de Vries P, Flanagan J, Frassinetti L, Frigione D, Giroud C, Groth M, Hawkes N, Hobirk J, Lehnen M, Maddison G, Mailloux J, Maggi C F, Matthews G, Mayoral M, Meigs A, Neu R, Nunes I, Puetterich T, Rimini F, Sertoli M, Sieglin B, Sips A C C, van Rooij G, Voitsekhovitch I and JET-EFDA Contributors 2014 *Nuclear Fusion* **54** 013011 ISSN 0029-5515

[31] Beurskens M N A, Frassinetti L, Challis C, Giroud C, Saarelma S, Alper B, Angioni C, Bilkova P, Bourdelle C, Brezinsek S, Buratti P, Calabro G, Eich T, Flanagan J, Giovannozzi E, Groth M, Hobirk J, Joffrin E, Leyland M J, Lomas P, de la Luna E, Kempenaars M, Maddison G, Maggi C, Mantica P, Maslov M, Matthews G, Mayoral M L, Neu R, Nunes I, Osborne T, Rimini F, Scannell R, Solano E R, Snyder P B, Voitsekhovitch I, de Vries P and JET-EFDA contributors 2014 *Nuclear Fusion* **54** 043001 ISSN 0029-5515

[32] Solano E R, Vianello N, Delabie E, Hillesheim J C, Buratti P, Réfy D, Balboa I, Boboc A, Coelho R, Sieglin B, Silburn S, Drewelow P, Devaux S, Dodt D, Figueiredo A, Frassinetti L, Marsen S, Meneses L, Maggi C F, Morris J, Gerasimov S, Baruzzo M, Stamp M, Grist D, Nunes I, Rimini F, Schmuck S, Lupelli I, Silva C and JET Contributors 2017 *Nuclear Fusion* **57** 022021

[33] Calabrò G, McDonald D C, Beurskens M, Maggi C F, Day I, de la Luna E, Eich T, Fedorczak N, Frigione D, Ford O, Giovanozzi E, Giroud C, Gohil P, Kiviniemi T P, Lennholm M, Lomas P J, Lonnroth J, Maddison G P, Nunes I, Pericoli Ridolfini V, Ryter F, Saibene G, Sartori R, Studholme W, Surrey E, Voitsekhovitch I, Zastrow K D and JET-EFDA Contributors 2010 H-mode threshold studies in helium-4 JET plasmas *Proceedings of the 37th EPS Conference on Controlled Fusion and Plasma Physics, Dublin, 2010* O5.127 URL `http://ocs.ciemat.es/EPS2010PAP/pdf/O5.127.pdf`

[34] Solano E R, Vianello N, Burrati P, Alper B, Coelho R, Delabie E, Devaux S, Dodt D, Figueiredo A, Frassinetti L, Howell D, Lerche E, Maggi C F, Manzanares A, Martin A, Morris J, Marsen S, McCormick K, Nunes I, Réfy D, Rimini F, Sirinelli A, Sieglin B, Zoletnik S and JET-EFDA Contributors 2013 M-mode: axi-symmetric magnetic oscillation and ELM-less H-mode in JET *Proceedings of the 45th EPS Conference on Controlled Fusion and Plasma Physics, Helsinki, 2013* P4.111 URL `http://ocs.ciemat.es/EPS2013PAP/pdf/P4.111.pdf`

[35] Conway G D, Angioni C, Ryter F, Sauter P, Vicente J and ASDEX Upgrade Team 2011 *Physical*

Review Letters **106** 065001 ISSN 0031-9007

[36] Birkenmeier G, Cavedon M, Conway G D, Manz P, Fuchert G, Laggner F M, Happel T, Medvedeva A, Nikolaeva V, Prisiazhniuk D, Shao L M, Maraschek M, Pütterich T, Ryter F, Willensdorfer M, Wolfrum E, Stroth U, Zohm H and the ASDEX Upgrade Team 2015 Characterisation of Pulsations Close to The L–H Transition in AUG *Proceedings of the 43rd EPS Conference on Controlled Fusion and Plasma Physics, Lisbon, 2015* P1.023 URL `http://ocs.ciemat.es/EPS2016PAP/pdf/P1.023.pdf`

[37] Xu G S, Wang H Q, Xu M, Wan B N, Guo H Y, Diamond P H, Tynan G R, Chen R, Yan N, Kong D F, Zhao H L, Liu A D, Lan T, Naulin V, Nielsen A H, Rasmussen J J, Miki K, Manz P, Zhang W, Wang L, Shao L M, Liu S C, Chen L, Ding S Y, Zhao N, Li Y L, Liu Y L, Hu G H, Wu X Q and Gong X Z 2014 *Nuclear Fusion* **54** 103002

[38] Cheng J, Dong J Q, Itoh K, Yan L W, Xu M, Zhao K J, Hong W Y, Huang Z H, Ji X Q, Zhong W L, Yu D L, Itoh S I, Nie L, Kong D F, Lan T, Liu A D, Zou X L, Yang Q W, Ding X T, Duan X R and Liu Y 2013 *Physical Review Letters* **110**

[39] Birkenmeier G, Cavedon M, Conway G D, Manz P, Stroth U, Fischer R, Fuchert G, Happel T, Laggner F M, Maraschek M, Medvedeva A, Nikolaeva V, Prisiazhniuk D, Pütterich T, Ryter F, Shao L M, Willensdorfer M, Wolfrum E, Zohm H and the ASDEX Upgrade Team 2016 *Nuclear Fusion* **56** 086009 ISSN 0029-5515

[40] Réfy D I, Solano E R, Vianello N, Zoletnik S, Dunai D, Tál B, Brix M, Gomes R, Birkenmeier G, Wolfrum E, Laggner F, Delabie E, the ASDEX Upgrade Team, the JET Contributors and the EUROfusion MST1 Team 2016 Comparative analysis of density profile and magnetic signals during the JET M-mode and ASDEX Upgrade I-phase phenomena *Proceedings of the 43rd EPS Conference on Controlled Fusion and Plasma Physics, Leuven, 2016* P1.125 URL `http://ocs.ciemat.es/EPS2015PAP/pdf/P1.125.pdf`

[41] Ryter F, Orte L B, Kurzan B, McDermott R M, Tardini G, Viezzer E, Bernert M, Fischer R and The ASDEX Upgrade Team 2014 *Nuclear Fusion* **54** 083003 ISSN 0029-5515

[42] Martin Y R, Takizuka T and The ITPA CDBM H-mode Threshold Data Group 2008 *Journal of Physics: Conference Series* **123** 012033 ISSN 1742-6596

[43] Delabie E, Maggi C, Cavedon M, Ryter F, Hughes J, McDonald D and Thomsen K 2018 Status of TC-26: L-H/H-L scaling in the presence of metallic walls, Scaling of the JET-ILW L-H threshold power in vertical target configuration, Report on TC-26 presented at the 21st T&C ITPA meeting (2018)

[44] Pereverzev G and Yushmanov P N 1991 ASTRA Automated System of TRansport Analysis in a Tokamak Tech. Rep. IPP-Report 5/42 Max-Planck-Institut für Plasmaphysik, Garching, Germany

[45] Staebler G M, Kinsey J E and Waltz R E 2007 *Physics of Plasmas* **14** 055909 ISSN 1070-664X

[46] Fable E, Angioni C, Casson F J, Told D, Ivanov A A, Jenko F, McDermott R M, Medvedev S Y, Pereverzev G V, Ryter F, Treutterer W, Viezzer E and The ASDEX Upgrade Team 2013 *Plasma Physics and Controlled Fusion* **55** 124028 ISSN 0741-3335

[47] Staebler G M, Howard N T, Candy J and Holland C 2017 *Nuclear Fusion* **57** 066046 ISSN 0029-5515

[48] Bonanomi N, Mantica P, Citrin J, Giroud C, Lerche E, Sozzi C, Taylor D, Tsalas M, Eester D V and JET Contributors 2018 *Nuclear Fusion* **58** 026028 ISSN 0029-5515

[49] Dominguez R R and Rosenbluth M N 1989 *Nuclear Fusion* **29** 844–848 ISSN 0029-5515

[50] Frigione D, Romanelli M, Challis C, Citrin J, Frassinetti L, Graves J, Hobirk J, Koechl F, Mantsinen M, Marin M, Mazzotta C, Pucella G and JET Contributors 2018 Impact of neon injection on electron density peaking in JET hybrid plasmas *27th IAEA Fusion Energy Conference, Ahmedabad, India* P/233

[51] Romanelli M, Frigione D, Challis C, Frassinetti L, Giroud C, Graves J, Hobirk J, Koechl F, Mantsinen M, Marin M, Menmuir S, Mazzotta C, Pucella G and JET Contributors 2018 Electron density peaking induced by neon seeding in jet hybrid plasmas *23rd Joint EU-US Transport Task*

Force Meeting, Seville, Spain URL `http://ocs.ciemat.es/EPS2014PAP/pdf/P1.031.pdf`

[52] Schweinzer J, Beurskens M, Frassinetti L, Joffrin E, Bobkov V, Dux R, Fischer R, Fuchs C, Kallenbach A, Hopf C, Lang P T, Mlynek A, Pütterich T, Ryter F, Stober J, Tardini G, Wolfrum E, Zohm H, The EUROfusion MST1 Team and The ASDEX Upgrade Team 2016 *Nuclear Fusion* **56** 106007 ISSN 0029-5515

[53] Sertoli M, Flanagan J, Maslov M, Maggi C, Coffey I, Giroud C, Menmuir S, Carvalho P, Shaw A, Delabie E and JET Contributors 2018 *Review of Scientific Instruments* **89** 113501 ISSN 0034-6748

[54] Sertoli M, Carvalho P, Giroud C, Menmuir S and JET Contributors 2019 *To be submitted to J. Plasma Phys.*

[55] Reimold F, Wischmeier M, Bernert M, Potzel S, Coster D, Bonnin X, Reiter D, Meisl G, Kallenbach A, Aho-Mantila L, Stroth U and ASDEX Upgrade Team 2015 *Journal of Nuclear Materials* **463** 128–134 ISSN 0022-3115

[56] Reimold F, Wischmeier M, Bernert M, Potzel S, Kallenbach A, Müller H W, Sieglin B, Stroth U and the ASDEX Upgrade Team 2015 *Nuclear Fusion* **55** 033004 ISSN 0029-5515